Chemical Composition-Dependent Hygroscopic Behavior of Individual Ambient Aerosol Particles Collected at a Coastal Site

Li Wu[1,2,+], Hyo-Jin Eom[1,3,+], Hanjin Yoo[1,4], Dhrubajyoti Gupta[1], Hye-Rin Cho[1], Pingqing Fu[2], and Chul-Un Ro[1,4,*]

[1] Department of Chemistry, Inha University, Incheon 22212, Korea

[2] Institute of Surface-Earth System Science, School of Earth System Science, Tianjin University, Tianjin 300072, China

[3] Air Quality Research Division, National Institute of Environmental Research, Incheon 22689, Korea

[4] Particle Pollution Management Center, Inha University, Incheon 21999, Korea

Correspondence to Chul-Un Ro (curo@inha.ac.kr)

[+]Authors with equal contributions

Abstract

This study investigated the hygroscopic behavior of individual ambient aerosol particles collected at a coastal site of Jeju Island, Korea. The particles' size change along with phase transitions during humidification and dehydration processes, and their chemical compositions, were determined by optical microscopy and scanning electron microscopy-energy dispersive X-ray spectroscopy (SEM-EDX), respectively. Of the 39 particles analyzed, 24 were aged sea-spray aerosols (SSAs) with diverse mixing ratios of Cl^- and NO_3^-.

The ambient SSAs exhibited multiple deliquescence and efflorescence transitions that were dominantly influenced by $NaCl$, $NaNO_3$, $MgCl_2$, $Mg(NO_3)_2$ and organic species covering the surface of the aged SSAs. For Cl-rich SSAs with $X_{(Na, Mg)Cl} > 0.4$, although some particles showed very slow water uptake at low RHs = ~30%, two major transitions were observed during the humidification process, firstly at RH = ~63.8%, regardless of their chemical compositions, which is the mutual deliquescence relative humidity (MDRH), and secondly at RH = 67.5–73.5%, depending on their chemical compositions, which are the final DRHs. During the dehydration process, the Cl-rich SSAs showed single-stage efflorescence at RH = 33.0–50.5%, due to simultaneous heterogeneous

31 crystallization of inorganic salts. For Cl-depleted SSAs with $X_{(Na, Mg)Cl} < 0.4$, two prompt deliquescence

32 transitions were observed during the humidification process, firstly at MDRH = 63.8 % and secondly

33 at RH = 65.4–72.9%. The mutual deliquescence transition was more distinguishable for Cl-depleted

34 SSAs. During the dehydration process, step-wise transitions were observed at efflorescence RHs (ERHs)

35 = 24.6–46.0% and 17.9–30.5%, depending on their chemical compositions.

36   Additionally, aged mineral particles showed partial or complete phase changes with varying

37 RH due to the presence of SSAs and/or NO_3^- species. In contrast, non-reacted mineral and Fe-rich

38 particles maintained their size during the entire hygroscopic process. The mixture particles of organic

39 and ammonium sulfate (AS) exhibited lower deliquescence and efflorescence RHs compared to pure

40 AS salt, highlighting the impact of organic species on the hygroscopic behavior of AS. These findings

41 emphasize the complexity of atmospheric aerosols and the importance of considering their composition

42 and mixing state when modeling their hygroscopic behavior and subsequent atmospheric impacts.

43

1 Introduction

45   Atmospheric aerosols play a significant role in the global climate by directly scattering or

46 absorbing incoming solar radiation and indirectly serving as cloud condensation nuclei (Haywood and

47 Boucher, 2000; Pandis et al., 1995). The hygroscopicity of ambient aerosol particles, critically

48 depending on their compositions, is of vital importance in understanding their properties, including

49 their effects on aerodynamic performance, cloud-droplet nucleation efficiency, optical properties, and

50 heterogeneous chemical reactivity with atmospheric gas-phase species (Krueger et al., 2003; ten Brink,

51 1998; Wang and Martin, 2007; Wu et al., 2020). However, the study of their hygroscopic behavior is

52 challenging because ambient aerosols typically exist as complex mixtures of several chemical species,

53 even at the individual particle level, due to multiphase interactions (Krieger et al., 2012; Pöschl and

54 Shiraiwa, 2015; Schiffer et al., 2018).

55   Sea-spray aerosols (SSAs) are a significant component comprising 25-60% of atmospheric

56 particulate matter mass (Finlayson-Pitts and Pitts, 2000; Song et al., 2022). Understanding the

57 hygroscopic properties of SSAs is essential for study on aerosol-cloud interactions and global climate

58 (Schill et al., 2015; Zieger et al., 2017), which however, is still defective owing to their complex

59 chemical compositions (Cochran et al., 2017; Meskhidze et al., 2013; Xu et al., 2020). Nascent SSAs

60 are formed when bubbles burst at the sea surface, generating both submicron and supermicron SSAs

61 from film and/or jet drops (Quinn et al., 2015; Wang et al., 2017). The primary inorganic constituents

62 of nascent SSAs are Na^+, Cl^-, and Mg^{2+}, followed by SO_4^{2-}, Ca^{2+}, K^+, and other minor compositions

63 (Seinfeld and Pandis, 2006). Submicron nascent SSAs contain more organic species and fewer

64 inorganic salts than supermicron ones (Ault et al., 2013; Prather et al., 2013; Wang et al., 2015). In

65 pristine marine environments, the organics in SSAs mostly originate from phytoplankton activities in

66 the sea, while in polluted marine environments, non-biodegradable surfactants from anthropogenic

67 waste run-offs to the sea are supposed to be added (Cochran et al., 2016; Forestieri et al., 2016).

68 Reactions of SSAs with various atmospheric species, such as NO_x/HNO_3, SO_2/H_2SO_4, and CH_3SO_3H,

69 within minutes to hours of residence in air further increase the complexity of the chemical compositions

70 (Liu et al., 2007; Saul et al., 2006; ten Brink, 1998), leading to partially or fully reacted (or aged) SSAs

71 after Cl depletion (Ault et al., 2014; Gard et al., 1998; Laskin et al., 2012; Pósfai et al., 1995; Wu et al.,

72 2020). The further reactive uptake of N_2O_5 was also reported to be dependent on the chloride to nitrate

73 ratio of the reacted SSAs and their phases (Ryder et al., 2014). In addition, SSAs interact with volatile

74 organic carbons (VOCs), secondary organic aerosols (SOAs), etc., in the marine boundary layer (Su et

75 al., 2022). The presence of primary and secondary organics, biogenic species, sea-salt sulfates (ss-

76 SO_4^{2-}), non-sea-salt sulfates (nss-SO_4^{2-}), etc., adds greater complexity to the interdependence of

77 hygroscopic behavior and heterogeneous reactions in ambient SSAs (Ault et al., 2013; Beardsley et al.,

78 2013; Keene et al., 2007; O'dowd and De Leeuw, 2007; Prather et al., 2013).

79   Many studies have investigated the hygroscopic behavior of both airborne and laboratory-

80 generated SSAs. It is generally accepted that sea-salt-containing particles result in higher hygroscopic

81 factors in supermicron particles (Atkinson et al., 2015; Herich et al., 2009). Some single particle

82 measurements have been reported on ambient fine and coarse mode SSAs that are dominated by

83 inorganic salt species. For example, environmental transmission electron microscopy was used to

84 measure the deliquescence and efflorescence relative humidities (DRHs and ERHs) of NaCl-bearing

85 aerosols, sulfate/chloride containing SSAs, Mg-rich particles, etc., collected from clean and polluted

86 environments (Semeniuk et al., 2007; Wise et al., 2007). It was found that NaCl moiety in

87 sulfate/chloride containing SSAs underwent deliquescence at ~75% RH with the sulfate-bearing phases

88 remaining insoluble, which is similar to the DRH of pure NaCl aerosols, whereas the DRH of the NaCl

89 moiety was lowered in the presence of soluble compositions like $NaNO_3$. In a follow-up study, the

90 DRHs and ERHs of laboratory-generated and ambient SSA particles were found to be consistent (Wise

91 et al., 2009). Similar observations for marine aerosols with insoluble sulfate moieties and a highly

92 hygroscopic NaCl-moiety were also reported (Freney et al., 2010). In-situ Raman spectrometry was

93   used to probe the phase transitions of SSA droplets (80–100 μm) nebulized from sea-water, which
94   revealed that $CaSO_4 \cdot 0.5H_2O$ solidified at RH > 90%, followed by crystallizations of NaCl and
95    $KMgCl_3 \cdot 6H_2O$ at RH = ~55% and ~44%, respectively (Xiao et al., 2008). Optical microscopy
96   combined with low-Z particle energy-dispersive electron probe X-ray microanalysis (low-Z particle
97   EPMA) was used to determine 2-D growth factors, phase transition RHs, and chemical compositions
98   in ambient aerosols, including nascent and reacted/aged SSAs (Ahn et al., 2010). However, the
99   relationship between hygroscopic properties and the evolving chemical compositions and mixing states
100   of ambient SSAs remains unclear.

101   Laboratory-generated inorganic salt particles have been utilized as surrogates to understand and
102   parameterize the complex hygroscopic properties of SSAs for climate models. Since NaCl constitutes
103   approximately 80% of nascent SSAs by mass, the hygroscopic behavior of pure NaCl particles has been
104   extensively studied for parameterizing the thermodynamic and optical properties and cloud activation
105   efficiency of ambient SSAs (Niedermeier et al., 2008; Tang et al., 1997). However, the hygroscopic
106   growth factors of ambient or laboratory-generated SSAs are reported to be different from those of pure
107   NaCl, possibly due to the presence of hydrates such as $MgCl_2 \cdot 6H_2O$, organic substances, or other
108   impurities (Ahn et al., 2010; Guo et al., 2019; Kong et al., 2018; Rosati et al., 2021; Schindelholz et al.,
109   2014; Zieger et al., 2017). Consequently, the hygroscopic properties of multicomponent systems such
110   as mixed cation chlorides (Chan et al., 2000; Ge et al., 1996, 1998; Gupta et al., 2015a; Li et al., 2014),
111   sodium salts of mixed anions (Chan et al., 1997; Chang and Lee, 2002; Freney et al., 2010; Gupta et
112   al., 2015b), and other mixture systems such as $NaCl-MgSO_4$ (Woods et al., 2010), $NaCl-CaSO_4$ (Freney
113   et al., 2010), $NaCl-(NH_4)_2SO_4$ (Tobon et al., 2021) are of special relevance, which can serve as
114   surrogates for ambient or reacted SSAs.

115   As discussed in detail elsewhere (Gupta et al., 2015a; Li et al., 2014), thermodynamic principles
116   predict stepwise phase transitions in two-component inorganic solid salt mixtures, such as NaCl-KCl,
117   $NaCl-MgCl_2$, and $NaCl-NaNO_3$, that can dissolve during the humidification process (Wexler and
118   Seinfeld, 1991). When the mixing ratio of the two-component is at a certain value, e.g. $X_{NaCl} = 0.38$ (or
119   $X_{NaNO_3} = 0.62$) in the $NaCl-NaNO_3$ mixture, particles act like a single-salt and exhibit a single phase
120   transition at its mutual DRH (MDRH), where the mixture is considered to have a eutonic composition.
121   For particles with other mixing ratios, the first transition generally occurs at their MDRH, regardless
122   of the specific ratios; and the resulting aqueous phase from partial deliquescence also possesses the
123   eutonic composition. As RH further increases, partially dissolved particles continue to absorb water

124 until the remaining solid component fully dissolves at the respective DRH, dependent on the salt moiety

125 richer in concentration. During the dehydration process, as RH decreases, the concentration of the richer

126 salt moiety becomes more concentrated, leading to crystallization at their respective ERH. The aqueous

127 phase of the eutonic composition then effloresces at their mutual ERH (MERH) as RH further decreases.

128   Thermodynamic models, such as the Extended Atmospheric Inorganics Model (E-AIM)

129 (http://www.aim.env.uea.ac.uk/aim/aim.php; (Ansari and Pandis, 1999; Carslaw et al., 1995; Clegg et

130 al., 1998b, a; Wexler and Clegg, 2002) and the Aerosol Inorganic-Organic Mixtures Functional groups

131 Activity Coefficients (AIOMFAC) (http://www.aiomfac.caltech.edu; Zuend et al., 2008, 2011), can

132 predict MDRHs and DRHs for multicomponent mixture systems. The DRH represents the solubility

133 limit (saturation concentration) of a compound in a solution, defining solid–liquid equilibrium. When

134 a solid compound coexists with a saturated liquid mixture, it has a specific molar ion activity product

135 (IAP) in that solution. The AIOMFAC model calculates IAP as a function of RH using ion activity

136 coefficients, which remains constant regardless of other mixture components. The corresponding RH

137 becomes the DRH when the calculated IAP matches that of saturated solutions. However, as

138 efflorescence is a kinetic or rate-driven process, no general theoretical model can predict the

139 efflorescence of single or multicomponent aerosol particles, and thus the best way is experimental

140 observation (Cohen et al., 1987; Martin et al., 2000). Previous modeling and field studies have

141 attributed the reduction in hygroscopic growth of SSAs to the organic fractions (Ming and Russell,

142 2001; Vaishya et al., 2013; Zhang et al., 2014), whereas recent measurements suggest that organic

143 species have an insignificant influence (Nguyen et al., 2017). Therefore, establishing a systematic

144 correlation between the chemical compositions and hygroscopic behavior of ambient SSAs vis-à-vis

145 the multicomponent inorganic surrogates is a priority towards understanding the hygroscopic properties

146 of ambient SSAs and parametrizing phase changes for model applications.

147   Mineral particles, such as aluminosilicates and calcium carbonate, which are typically non-

148 hygroscopic, can become hygroscopic when they are internally mixed with SSAs or react with gaseous

149 species such as NO_x, SO_2, and organic acids in the presence of water vapor (Li et al., 2014; Tang et al.,

150 2016). In fact, mineral dust and aged SSAs may exist as internal and/or external mixtures in the

151 atmosphere (Geng et al., 2014). For instance, Mg-silicate particle coagulated with SSA partially

152 increased in size only at the SSA region with increasing RH and was covered with an aqueous droplet

153 caused by the complete dissolution of the SSA part in high RH (Semeniuk et al., 2007). Additionally,

154   aluminosilicates coated with sulfur-bearing materials or internally mixed with sea salt particles can
155   absorb water, although the aluminosilicates remained as solid phases (Freney et al., 2010).

156   In this study, we systematically investigated the hygroscopic behavior of ambient aerosols
157   collected on Jeju Island, Korea, together with their chemical compositions in various mixing states on
158   a single particle basis. Especially, the hygroscopic properties and chemical compositions of ambient
159   SSAs were examined and compared with multicomponent inorganic surrogate systems containing Na^+,
160   Mg^{2+}, Cl^-, and NO_3^-. The phase transitions were observed by monitoring the 2-D size changes of the
161   particles as a function of RH under optical microscopy and the hygroscopic curves and phase diagrams
162   were derived. To determine the chemical compositions of the individual ambient aerosols and the
163   spatial distribution of elements in the effloresced particles, we used scanning electron
164   microscopy/energy dispersive X-ray spectroscopy (SEM/EDX) and analyzed their X-ray spectra and
165   maps, respectively. Although ambient aerosols are complex in their compositions and hygroscopic
166   properties, the detailed elucidation of their hygroscopic behavior according to chemical compositions
167   of ambient aerosols can contribute to the ongoing efforts to improve our understanding of atmospheric
168   aerosols and their impacts on global climate.

169

170   **2 Experimental Section**
171   **2.1 Samples**
172   **Ambient aerosol particles**

173   Aerosol samples were collected on April 16 and 17, 2012, at the Gosan meteorological site
174   (33.29°N, 126.16°E) located on the west coast of Jeju Island in South Korea (see Fig. 1). Ambient
175   aerosols were loaded on TEM grids (200-mesh Cu coated with Formvar stabilized with carbon, Ted
176   Pella, Inc.) mounted on stages 2 and 3 of a three-stage cascade PM_{10} impactor (Dekati Ltd.) with
177   aerodynamic cut-off diameters of 10–2.5 µm and 2.5–1.0 µm, respectively, at a flow rate of 10 L min$^-$
178   ^{1}. Sampling durations for each stage were adjusted to collect an appropriate number of particles without
179   overloading. The samples were put into black plastic boxes and sealed with parafilm immediately after
180   the collection and these sealed samples were then stored in a refrigerator before the measurements.
181   Stage 2 particles, which were sized between 10-2.5 µm, were used to measure chemical composition
182   and hygroscopic behavior in this study.

183

184   **Laboratory-generated (Na, Mg)(Cl, NO₃) mixture particles**

185   In the previous studies (Gupta et al., 2015a, b; Zhang et al., 2004), aerosols of NaCl, NaNO$_3$,

186   Mg(NO$_3$)$_2$, NaCl-NaNO$_3$, and NaCl-MgCl$_2$ were extensively investigated. As Na$^+$, Mg^{2+}, Cl$^-$, and NO$_3^-$

187   are major species of the ambient SSAs collected in our samples, based on low-Z particle EPMA results,

188   we measured the hygroscopic behavior of NaCl-MgCl$_2$-NaNO$_3$-Mg(NO$_3$)$_2$ surrogate system in this

189   work to simulate ambient SSAs that contain similar major elements. Pure solutions (1.0 M each) of

190   NaCl (>99.9% purity, Aldrich), MgCl$_2$·6H$_2$O, and NaNO$_3$ (99.9% purity, Aldrich) were prepared using

191   de-ionized water (18 MΩ, Millipore Direct-QTM). The pure solutions were then mixed to obtain

192   solutions with [Cl$^-$]:[NO$_3^-$] = 3:1, 1:1, and 1:3 (i.e. $X_{(Na,Mg)Cl}$ = 0.75, 0.5, and 0.25), while maintaining

193   the sea water ratio of [Na$^+$] : [Mg^{2+}] = 9:1 (Haynes, 2015), as the elemental ratio of Na and Mg in the

194   ambient SSAs from our samples is also approximately 9. A single jet atomizer (HCT4810) was used to

195   generate aerosol particles from the mixture solutions on hydrophobic TEM grids. Herein, a notation

196   system is used to represent aerosol particles of NaCl-MgCl$_2$-NaNO$_3$-Mg(NO$_3$)$_2$ as (Na, Mg)(Cl, NO$_3$).

197

198   **2.2 Hygroscopic property measurements**

199   The experimental setup for measuring hygroscopic behavior consists of three main components:

200   (A) a see-through impactor, (B) an optical microscope, and (C) a humidity control system. The TEM

201   grid with aerosol particles was attached to the impaction plate in the see-through impactor, and the RH

202   was controlled by mixing dry and wet gaseous N$_2$ (99.999% purity) flows that were adjusted to obtain

203   the desired RH in the range of ~5.0−92.0%. The humidity control system used wet N$_2$ gas obtained by

204   bubbling through deionized water reservoirs. The RH was monitored by a digital hygrometer (Testo

205   645) that was calibrated using a dew-point hygrometer (M2 Plus-RH, GE) to provide RH readings with

206   ±0.5% reproducibility. A detailed discussion of the impactor and humidity-controlling system can be

207   found elsewhere (Li et al., 2021). The particles were continuously imaged in RH = 1% steps using a

208   digital camera (Canon EOS 5D, full frame, Canon EF f/3.5 L macro USM lens) mounted on an optical

209   microscope (Olympus, BX51M) during the humidification process (by increasing RH from ~5.0 to

210   92.0 %), followed by the dehydration process (by decreasing RH from ~92.0 to 5.0 %). The changes in

211   particle size with the variation of RH were monitored by measuring the particle areas in the optical

212   images to generate hygroscopic curves. Each humidity condition was sustained for at least 2 mins to

213   allow for sufficient time for water condensation or evaporation. The hygroscopic curves are represented

214   by the area ratio (A/A_0) as a function of RH, where the 2-D projected aerosol area at a given RH (A) is

215   divided by that before starting the humidification process (A_0). The images were processed using image

216   analysis software (Matrox, Inspector v9.0). The experiments were conducted at room temperature (T =
217   22 ± 1 °C). Pure NaCl particles were used to verify the accuracy of the system with DRH = 75.5 (±
218   0.5) % and ERH = 46.3–47.6 %.

219

220   **2.3 Low-*Z* particle EPMA measurements using SEM-EDX**

221   The ambient aerosol particles were analyzed using low-*Z* particle EPMA measurements with a
222   Jeol JSM-6390 SEM equipped with an Oxford Link super atmospheric thin window (SATW) EDX
223   detector. The analysis was conducted both before and after the hygroscopic processes to find out fields
224   on TEM grids with well-separated particles based on their secondary electron images (SEIs, ~ 100 μm
225   x 100 μm for a field) and to determine the morphology, chemical composition, and spatial distribution
226   of the chemical elements (elemental maps), respectively. The resolution of the detector was 133 eV for
227   Mn Kα X-rays. Point mode and area mode X-ray spectra and elemental maps of individual particles
228   were recorded using Oxford INCA Energy software. An accelerating voltage of 10 kV and beam current
229   of 0.5 nA were used, and typical measurement durations were 20 sec. for point mode, 1 min. for area
230   mode, and 5-10 min. for elemental mapping.

231   The AXIL program was used to obtain the net X-ray intensities for chemical elements through
232   non-linear least-squares fitting of the spectra. From these intensities, the elemental concentrations of
233   individual particles were determined (Vekemans et al., 1994). For individual particles sitting on TEM
234   grids, C and O concentrations were determined using a Monte Carlo calculation technique to correct
235   for the interfering X-ray peaks of C and O emitted from the TEM grid, providing accurate quantification
236   results (Geng et al., 2010). A detailed explanation of the elemental quantification procedure can be
237   found elsewhere (Wu et al., 2019).

238

239   **3 Results and Discussion**

240   **3.1 Chemical composition and hygroscopic behavior of individual ambient aerosol particles**

241   In this study, a total of 39 particles on three fields were investigated, including 24 aged/reacted
242   SSAs with diverse mixing ratios of Cl^- and NO_3^- and 15 other particles such as six aluminosilicates,
243   five Ca-containing particles, two Fe-rich particles, an aged SiO_2, and a mixture particle of organic and
244    $(NH_4)_2SO_4$. The mole fraction of Cl as $X_{(Na,Mg)Cl}$ in the aged/reacted SSAs was calculated based on
245    $[Cl^-]/([Na^+]+2[Mg^{2+}])$ to determine the degree of Cl-depletion in the SSA particles. Fig. 2 shows the
246   SEI of the first field containing 16 particles, where the chemical species of each particle are indicated,

247   together with two exemplar X-ray spectra of aged SSAs #5 and #11 with $X_{(Na,Mg)Cl}$ = 0.75 and 0.23,

248   respectively. The elemental concentrations of all particles and their chemical species, determined by X-

249   ray spectral analysis, are listed in Table S1 of Supporting Information.

250   In Fig. 3, optical images obtained at different RHs during the humidification and dehydration

251   processes and the secondary electron image (SEIs) after hygroscopic process for 16 particles on the

252   first field are shown. Except particles #2, #4, #7, #8, and #14, the rest are aged SSAs. Optical images

253   and the SEIs for particles on the second and third fields are provided in Figs. S1 and S2, respectively.

254   Particles were initially solid at RH = 5.3 % before the hygroscopic measurement, as shown in Fig. 3A.

255   During the humidification process, most of the SSAs showed partial deliquescence at RH = 63.8 %

256   (Fig. 3C), regardless of their aging degree, indicating the realization of the MDRH. Upon further

257   increase of RH, SSAs underwent full deliquescence transitions at DRH = 65.4 – 73.5 %, which varied

258   for each SSA, as shown in Figs. 3D and E. During the dehydration process, almost all SSAs exhibited

259   colored ring-type patterns (Figs. 3G and H) due to the diffraction of visible light typically observed in

260   the presence of organic surfactants on water, indicating the presence of considerable amounts of organic

261   species in aged SSAs. SSA droplet #5 crystallized at ERH = 50.5 % (Fig. 3G), while the others

262   effloresced over a lower range of ERH = 46.0 – 17.9%. The various DRHs and ERHs indicate different

263   chemical compositions of SSAs.

264   Aluminosilicates and Fe-rich particles did not exhibit any water uptake or changes as a function

265   of RH. Aged aluminosilicates, aged SiO_2, and some reacted Ca-containing particles showed modest

266   growth/shrinkage continuously due to the presence of amorphous NO_3^- phases (Ahn et al., 2010). The

267   mixture particle of organic and ammonium sulfate experienced distinct deliquescence and efflorescence.

268   Detailed description of hygroscopic behavior of the ambient aerosol particles is given as follows.

269

270   **3.2 SSA particles**

271   The average atomic concentrations of C, Na, Cl, N, Mg, S, K, and Ca in SSAs are listed in Table

272   S1 with the values being 43.0(±7.2)%, 13.6(±4.6)%, 8.0(±6.6)%, 7.9(±2.3)%, 1.5(±0.4)%, 0.8(±0.3)%,

273   0.3(±0.1)%, and 0.3(±0.1)%, respectively. The elemental analysis of the SSAs indicates that they

274   consist primarily of Na^+, Mg^{2+}, Cl^-, NO_3^-, and organic species. The elemental concentration of N is

275   significantly higher than that of S, and the elemental ratio of S and Na in the ambient SSAs collected

276   from our samples closely resembles that of sea water ([S]/[Na] = 0.06; Haynes, 2015). As a result, the

277   SSAs is considered to contain more nitrate due to the rapid reaction with NO_x/HNO_3, as opposed to

278   sulfate. As the SSAs become more aged or reacted, their mole fractions of Cl$^-$ relative to Na$^+$ and Mg^{2+}

279   decrease, while their mole fractions of NO$_3^-$ increase. Although the aged/reacted SSAs are a

280   complicated multi-component system as a fraction of ambient aerosols, (Na, Mg)(Cl, NO$_3$) mixture

281   system is considered as an inorganic surrogate system for understanding their hygroscopic behavior.

282   The AIOMFAC model predicts the eutonic compositions of Na(Cl, NO$_3$) and (Na, Mg)(Cl, NO$_3$)

283   mixture systems as X_{NaCl} = 0.38 and $X_{(Na,Mg)Cl}$ = 0.46, respectively. The mole fraction of Cl in the

284   eutonic compositions of the inorganic component of the aged SSAs would be around 0.4. And thus, the

285   SSAs can be classified as Cl-rich or Cl-depleted depending on their $X_{(Na,Mg)Cl}$ values being greater or

286   less than 0.4, respectively.

287

288   **3.2.1 Cl-rich SSAs**

289   Fig. 4 displays the projected 2-dimensional (2-D) area ratio and optical images for Cl-rich SSAs

290   #5 and #19 (panels a and d, respectively), and the 2-D area ratio of humidification (panels b and e) and

291   dehydration (panels c and f) for the two SSAs as a function of RH. For SSAs #5 and #19 the mole

292   fraction of chloride, $X_{(Na,Mg)Cl}$ was calculated to be 0.75 and 0.72, respectively. In addition, the figure

293   also includes the (Na, Mg)(Cl, NO$_3$) particle with $X_{(Na,Mg)Cl}$ = 0.75 for comparison.

294   During the humidification process, SSAs #5 and #19 initially remained constant in size until

295   RH reached around 30%, after which they gradually increased in size. This behavior is also consistent

296   with the (Na, Mg)(Cl, NO$_3$) system (Figs. 4b and e), suggesting that MgCl$_2$·6H$_2$O (DRH = 33.3 %) or

297   Mg^{2+}-rich eutonic part may have undergone water absorption (Gupta et al., 2015a; Zieger et al., 2017).

298   However, the deliquescence transitions were not as distinct as those in particles with $X_{(Na,Mg)Cl}$ = 0.25

299   and 0.5 generated from (Na,Mg)(Cl,NO$_3$) mixture solutions (see Fig. S3 in the Supporting Information).

300   The size increase was followed by a shrinkage until RH = 60.5% due to structural rearrangement in the

301   remaining undissolved salt-mixture crystals. Structural rearrangements are commonly observed after

302   preliminary absorption of water at RHs just before the prompt deliquescence transition (Ahn et al.,

303   2010; Gupta et al., 2015a,b; Mikhailov et al., 2009). At first DRH = 63.8%, a partial droplet-like shape

304   appeared in the particle morphology although there was no significant change in the 2-D area ratio.

305   Clear final deliquescence transitions were observed in both SSAs #5 and #19 at DRHs = 73.5 % and

306   72.9 %, respectively, due to the dissolution of the remaining solid NaCl moiety in these Cl-rich particles.

307   The measured DRHs of SSAs #5 and #19 were closer to the final DRHs calculated for the Na(Cl, NO$_3$)

308   system using the AIOMFAC model (Fig. 6), and higher than the calculated and measured ones in the

309 (Na, Mg)(Cl, NO$_3$) particles (Figs. 4b and e and Fig. 6). These observations for the Cl-rich SSAs suggest

310 that most of the Mg^{2+} salts (MgCl$_2$·6H$_2$O with DRH = 33.3 %; Mg(NO$_3$)$_2$ with DRH = 52%) have

311 already dissolved at low RHs or undergone complexation with organic moieties (Eom et al., 2016), and

312 the remaining NaCl and NaNO$_3$ moieties drove the deliquescence transition. The hygroscopic growth

313 of both SSAs #5 and #19 was much smaller than that of the (Na, Mg)(Cl, NO$_3$) system (Figs. 4b and e)

314 when RH was raised to 91.4%, indicating the presence of a partitioning hydrophobic layer composed

315 of organic surfactants that covered the aqueous salt droplets and inhibited water uptake (Bertram et al.,

316 2018; Cochran et al., 2016; Eom et al., 2016; Lee et al., 2020).

317   During the dehydration process as RH decreased from ~91% to ~5%, both the SSA droplets

318 showed a continuous shrinkage in size before their efflorescence. However, the rate of shrinkage was

319 much smaller than that of pure inorganic surrogates, such as the (Na, Mg)(Cl, NO$_3$) system with

320 $X_{(Na,Mg)Cl}$ = 0.75 (Figs. 4c and f), indicating that the hydrophobic surfactant layers covering the aqueous

321 salt droplets potentially impeded the water evaporation. SSAs #5 and #19 showed one clear

322 efflorescence transition at RH = 50.5% and 45.0%, respectively (Figs. 4a and d). Interestingly, SSA #5

323 ($X_{(Na,Mg)Cl}$ = 0.75) underwent a sharp decrease in size from RH = 50.9 – 50.5%, which is considerably

324 higher than the ERH range of ~45 – 47% for pure NaCl particles (Ahn et al., 2010; Eom et al., 2014;

325 Martin, 2000), and the first ERHs of either Na(Cl, NO$_3$) (Fig. 7) or (Na, Mg)(Cl, NO$_3$) (Figs. 4c and 7)

326 systems. On the other hand, SSA #19 ($X_{(Na,Mg)Cl}$ = 0.72) first showed a small decrease in size at RH =

327 63.8 – 60.8%, which is not a typical efflorescence transition, followed by a sharp decrease in size at

328 RH = 45.8 – 45.0%, which is on the lower side of the ERH range for pure NaCl and slightly higher

329 than the first ERHs of Na(Cl, NO$_3$) and (Na, Mg)(Cl, NO$_3$) systems (Figs. 4f and 7). The higher ERH

330 at RH = 50.5 % in SSA #5 indicates heterogeneous efflorescence of the NaCl moiety, while the ERH =

331 45.0% in SSA #19 suggests the homogeneous nucleation of NaCl moiety. Both SSA droplets showed

332 just one decisive efflorescence transition at their ERHs, indicating co-crystallization of most aqueous

333 inorganic salt moieties along with NaCl, pointing towards the likelihood that the SSAs with more

334 complicated chemical compositions than the (Na, Mg)(Cl, NO$_3$) mixture aerosols contain chemicals

335 which can act as seeds, such as (Na, Ca)SO$_4$ crystals, for the complete crystallization at the

336 efflorescence transition. These observations are substantiated by the distribution of S and O at the center

337 and edge of the NaCl moiety in the X-ray maps obtained from the effloresced SSA particles #5 and #19,

338 respectively (Fig. S4) (Li et al., 2014; Gupta et al., 2015a). The apparent (not so sharp) decrease in size

339 of SSA #19 at RH = 63.8 – 60.8% could be attributed to: (i) the sudden shrinkage of viscous organic

340   moieties covering the aqueous salt droplet; or (ii) inhibited or slow water loss, probably due to a kinetic

341   barrier to crystallization from amorphous/gel forming moieties such as

342    $MgSO_4/Mg(NO_3)_2/(CH_3SO_3)_2(Mg, Ca)$ (Liu and Laskin, 2009; Xiao et al., 2008; Zhang et al., 2004;

343   Zhao et al., 2006); or (iii) a phase transition, such as heterogeneous efflorescence, had occurred, but

344   the presence of viscous moieties (organics or Mg^{2+}- organic complex) affected the relative 2-D size

345   decrease on the TEM grid substrate.

346

347   **3.2.2 Equimolar and Cl-depleted SSAs**

348   Fig. 5 shows the plots of the projected 2-D area ratio and optical images for an equimolar SSA

349   #23 (Fig. 5a) and a Cl-depleted SSA #11 (Fig. 5d), and 2-D area ratio of humidification (panels b and

350   e) and dehydration (panels c and f) for the two SSAs as a function of RH. The calculated mole fractions

351   of chloride, $X_{(Na, Mg)Cl}$ for SSAs #23 and #11 are 0.52 and 0.23, respectively. The figure also includes

352   the $(Na, Mg)(Cl, NO_3)$ particles with $X_{(Na, Mg)Cl} = 0.5$ and 0.25 for comparison.

353   During the humidification process, both SSAs #23 and #11 remained relatively constant until

354   RH = ~50 %, unlike the $(Na, Mg)(Cl, NO_3)$ system, probably due to the decreased concentration of

355    $MgCl_2·6H_2O$. The particle size then began to shrink until RH = ~59%. Both SSAs exhibited two distinct

356   deliquescence transitions. Partial deliquescence transitions occurred at RH = ~63.8%, which is the

357   MDRH for the mixture of soluble moieties in the ambient SSAs and was reported for the first time.

358   Both SSAs exhibited two clear deliquescence transitions. The observed and AIOMFAC-calculated

359   MDRHs of the $Na(Cl, NO_3)$ system are ~68%, while the AIOMFAC-calculated second MDRH for the

360    $(Na, Mg)(Cl, NO_3)$ system is 66.5% after the dissolution of $MgCl_2·6H_2O$ at the calculated first MDRH

361   of ~34%, as shown in Fig. 6. This indicates that the eutonic component in the ambient SSAs, with a

362   lower MDRH of 63.8%, is composed of $NaCl$, $NaNO_3$, $Mg(NO_3)_2$, and some other minor, less-soluble

363   moieties. The mutual deliquescence transition was more distinct in Cl-depleted SSAs than in Cl-rich

364   SSAs, suggesting that the eutonic component in the ambient SSAs is richer with other salts compared

365   to NaCl. As RH increased further, both SSAs #23 and #11 underwent final deliquescence transitions at

366   DRHs = 69.5%. The observed DRH for SSA #23 $(X_{(Na,Mg)Cl} = 0.52)$ is closer to the final DRH calculated

367   from AIOMFAC for pure NaCl moiety in the $Na(Cl, NO_3)$ system (Fig. 6), and higher than the

368   AIOMFAC-calculated final DRH for pure NaCl moiety in the $(Na, Mg)(Cl, NO_3)$ system (Figs. 5b and

369   6). The observed DRH for SSA #11 $(X_{(Na,Mg)Cl} = 0.23)$ is lower than the AIOMFAC-calculated final

370   DRH (Fig. 6) for pure $NaNO_3$ moiety in the $Na(Cl, NO_3)$ system (Gupta et al., 2015b), and close to the

371   AIOMFAC-calculated final DRH for pure $NaNO_3$ moiety in the $(Na, Mg)(Cl, NO_3)$ system (Figs. 5e

372   and 6). The observation of Cl-depleted SSAs during humidification suggests that a $(Na, Mg)(Cl, NO_3)$

373   dominant composition drives the deliquescence transition. As RH increased further, the hygroscopic

374   growth of both SSAs #23 and #11 was stunted, in comparison to the $(Na, Mg)(Cl, NO_3)$ mixture systems

375   (Figs. 5b and e), likely due to the presence of hydrophobic surfactants covering the aqueous salt droplet.

376   During the dehydration process, both SSAs #23 and #11 showed slower rates of shrinkage

377   compared to the $(Na, Mg)(Cl, NO_3)$ mixture systems (Figs. 5c and f), suggesting inhibition of water

378   evaporation due to surface hydrophobic organic moieties. The diffraction patterns at the aqueous salt

379   droplet-organic surfactant interface were more prominent in the form of color and/or ring-like patterns

380   for equimolar and Cl-depleted SSAs (Figs. 5a and d), indicating that the hydrophobic organic film may

381   become thicker, or the concentration of organic surfactants may increase with aging. During

382   dehydration, SSA #23, which is equimolar or slightly Cl-rich, showed one sharp transition at RH =

383   44.1-43.6% and a gradual decrease in size thereafter until RH = 30.7%, which is not considered an

384   efflorescence transition (Fig. 5a). The distinct ERH of 43.6% observed for SSA #23 was higher than

385   the first ERHs of both $Na(Cl, NO_3)$ and $(Na, Mg)(Cl, NO_3)$ systems (Fig. 5c and 7), indicating possible

386   homogeneous efflorescence of NaCl along with other salts on crystalline seeds such as $(Ca, Na)SO_4$

387   (Pósfai et al., 1995; Semeniuk et al., 2007; Wise et al., 2007), as shown in the X-ray maps in Fig. S5a.

388   The remaining metastable amorphous/gel type NO_3^- moieties and $MgSO_4 \cdot xH_2O$ may be responsible

389   for the gradual decrease in size after the efflorescence transition (Li et al., 2016). Cl-depleted SSA #11

390   showed two clear efflorescence transitions at RH = 44.1–39.6% and 24.6–23.9%, as shown in Fig. 5d.

391   The first ERH of 39.6% measured for SSA #11 was also higher than the ERHs for both $Na(Cl, NO_3)$

392   and $(Na, Mg)(Cl, NO_3)$ systems, while the second ERH of 23.9% was close to and lower than the ERH

393   range for pure NaCl in $(Na, Mg)(Cl, NO_3)$ and $Na(Cl, NO_3)$ systems, respectively (Figs. 5f and 7). The

394   observations for Cl-depleted SSA #11 suggest that the first ERH was most probably due to the

395   heterogeneous crystallization of the dominant $NaNO_3$ and/or $Mg(NO_3)_2$ on mixed cation sulfate

396   crystalline seeds such as $(Ca, Na)SO_4$, while NaCl continued to homogeneously nucleate until the

397   second ERH, where it crystallized at the center/core of the particle (Woods et al., 2013), as shown in

398   the X-ray maps in Fig. S5b.

399

400   **3.2.3 Phase diagrams of ambient SSAs in correlation with $Na(Cl, NO_3)$ and $(Na, Mg)(Cl, NO_3)$**

401   **surrogates systems**

The phase diagrams of ambient SSAs in correlation with Na(Cl, NO₃) and (Na, Mg)(Cl, NO₃) surrogate systems can show the relationship between the observed deliquescence and efflorescence behavior of the ambient SSAs and those of the two surrogate systems. The ambient SSAs have more complex compositions, but the simpler Na(Cl, NO₃) and (Na, Mg)(Cl, NO₃) surrogate systems can help to identify the dominant salts and their behavior in the ambient SSAs. For example, the observation of Cl-depleted SSAs during humidification suggests that a (Na, Mg)(Cl, NO₃) dominant composition drives the deliquescence transition. This information can be useful in understanding the hygroscopic properties and behavior of atmospheric aerosols.

3.2.3.1 Deliquescence phase diagram

Fig. 6 shows the experimentally measured DRHs for the ambient SSA particles and those of the (Na, Mg)(Cl, NO₃) and Na(Cl, NO₃) systems, calculated from the AIOMFAC model, plotted as a function of the mole fraction of chloride, $f(X_{(Na, Mg)Cl}$ or $X_{NaCl})$.

The first MDRH of the (Na, Mg)(Cl, NO₃) system, which was calculated from AIOMFAC, is 34.2%, and the MDRH measured in laboratory-generated (Na, Mg)(Cl, NO₃) particles is ~33.4% (Fig. S3). These values are attributed to the dominant $MgCl_2 \cdot 6H_2O$ eutonic component (Gupta et al., 2015a). In some Cl-rich SSAs, a gradual increase in size and a change in morphology were observed at RH = ~33%, indicating that they were in the partial aqueous phase (Figs. 4a and d). It is also possible that the gradual water uptake observed in SSAs at low RHs is due to amorphous inorganic moieties such as $MgSO_4 \cdot xH_2O$ (Xiao et al., 2008; Zhao et al., 2006) and $Mg(NO_3)_2 \cdot xH_2O$ (Zhang et al., 2004), and/or water-soluble secondary organics such as carboxylate salts formed due to reactions of the (Na, Mg)Cl species with dicarboxylic acids, which are ubiquitous in the marine boundary layer (Ghorai et al., 2014; Laskin et al., 2012; Li et al., 2021). Wise et al. (2009) reported that ambient SSAs started changing in morphology at 36(±15)% RH.

For the (Na, Mg)(Cl, NO₃) system, the eutonic composition is $X_{(Na,Mg)Cl} = 0.46$, with a second MDRH of 66.5%, calculated from AIOMFAC, and a measured value of ~66.6(±0.4)% in the laboratory-generated (Na, Mg)(Cl, NO₃) particles (Fig. S3). For the Na(Cl, NO₃) system, the eutonic composition is $X_{NaCl} = 0.38$, with the MDRH of 67.9%, calculated from AIOMFAC, and a measured value of ~67.9(±0.3)% in the laboratory-generated particles (Gupta et al., 2015b). The observed MDRH of 63.8(±0.3)% for the ambient SSAs (Fig. 6) is slightly lower than those of the Na(Cl, NO₃) and (Na, Mg)(Cl, NO₃) mixture systems, indicating that the eutonic component in the mutual deliquescence

transition may be Na(Cl, NO$_3$)-rich, with minor concentrations of other soluble salt moieties, as the MDRH of salt mixtures is generally lower than individual salt DRHs (Wexler and Seinfeld, 1991). It is less likely that Na$_2$SO$_4$ or CH$_3$SO$_3$Na are major components of the eutonic component in these ambient SSAs, as they have much higher MDRHs, i.e., MDRHs = 84.0% for Na(Cl, SO$_4$) and 71% for Na(Cl, CH$_3$SO$_3$) (Chang and Lee, 2002; Liu and Laskin, 2009; Liu et al., 2011). The lowest final DRH measured for SSA #1 with $X_{(Na,Mg)Cl}$ = 0.33 is at RH = 65.4 % (Fig. 6), which is close to the observed MDRH of 63.8($\pm$0.3)%, suggesting that the eutonic component likely has a chloride mole fraction within the range of $X_{(Na,Mg)Cl}$ = ~0.30–0.40. Interestingly, Wise et al. (2009) reported rounding in particle morphology at RH = 65($\pm$4)%, which is close to the observed MDRH but was not confirmed as such since only four ambient SSA particles were studied.

The final DRHs in both (Na, Mg)(Cl, NO$_3$) and Na(Cl, NO$_3$) systems are solely determined by the solid salt remaining after the mutual deliquescence of the eutonic component. Fig. 6 clearly shows that for the Cl-rich SSA particles with $X_{(Na,Mg)Cl}$ > 0.40, which contain more NaCl than the eutonic composition, the final DRH values (~67.5-73.5%) approached the DRH of pure NaCl salt (~75.3% at 298 K) as the chloride concentration increased. Similarly, for the Cl-depleted particles with $X_{(Na,Mg)Cl}$ < 0.40, the final DRH values (~65.4-72.9%) approached that of pure NaNO$_3$ salt (~74% at 298 K) as the chloride concentration decreased.

The chemical components of each phase in the ambient SSAs during the humidification process are not well known, therefore, five possible single and/or mixed phases are notated as alphabets (P, Q, R, S, and T) and the possible major chemical components in each phase (s = solid; aq = aqueous) are listed as follows:

(i) P-(s): all components are mixed in solid phase at RH < ~33–35% at all mole fractions of chloride.

(ii) Q-(s + aq): a mixed phase comprising possibly aqueous MgCl$_2$·6H$_2$O dominant eutonic components + solid NaCl, (Na, Mg, Ca)(NO$_3$, SO$_4$) and organics between RH = ~33% and the first clear MDRH of ~63.8%.

(iii) R-(s + aq): a mixed phase comprising solid NaNO$_3$ and (Ca, Na)SO$_4$ + aqueous eutonic components rich in Na(Cl, NO$_3$) and Mg(NO$_3$, SO$_4$, organics) between RH = 63.8% and final DRHs for $X_{(Na,Mg)Cl}$ < 0.40, i.e., Cl-depleted SSAs.

(iv) S-(s + aq): a mixed phase comprising solid NaCl and (Ca, Na)SO$_4$ + aqueous eutonic components rich in Na(Cl ,NO$_3$) and Mg(Cl, NO$_3$, SO$_4$, organics) between the RH = 63.8% and

463   final DRHs for $X_{(Na,Mg)Cl} > 0.40$, i.e., Cl-rich SSAs.

464   (v) T-(aq): aqueous phase for most components including NaCl, NaNO$_3$, and Mg(Cl, NO$_3$, SO$_4$,

465   organics) above the measured final DRHs at all mole fractions of chloride, while (Ca, Na)SO$_4$

466   should remain in crystalline solid phase and does not take part in the deliquescence transitions

467   in the measured RH range.

468

469   **3.2.3.2 Efflorescence phase diagram**

470   The experimentally measured ERHs for the ambient SSA particles and those of (Na, Mg)(Cl,

471   NO$_3$) and Na(Cl, NO$_3$) systems are plotted as a function of the mole fraction of chloride, f($X_{(Na,Mg)Cl}$ or

472   X_{NaCl}) in Fig. 7.

473   The first ERH values decrease from 44.5% to 24.8% and from 47.1% to 20.2% with decreasing

474   mole fractions of chloride for $X_{(Na, Mg)Cl} = 0.75$ to 0.25 in the (Na, Mg)(Cl, NO$_3$) and $X_{NaCl} = 0.9$ to 0.1

475   in the Na(Cl, NO$_3$) systems, respectively (Gupta et al., 2015b; Woods et al., 2013). This suggests that

476   the first efflorescence transitions in the Na(Cl, NO$_3$) and (Na, Mg)(Cl, NO$_3$) mixture systems are solely

477   due to the homogeneous nucleation of NaCl for both Cl-rich and Cl-depleted particles, and that the

478   amorphous (Na, Mg)NO$_3$ species cannot undergo homogeneous crystallization even at high

479   supersaturation (Kim et al., 2012; Zhang et al., 2004). In the case of Cl-rich ($X_{(Na,Mg)Cl} > 0.40$) ambient

480   SSAs, the first ERHs systematically decreased ranging from 50.5% to 33.0% due to the homogeneous

481   nucleation of NaCl for most particles. However, for a few particles, such as SSA #5 (Fig. 4a, ERH =

482   50.5%), NaCl underwent heterogeneous crystallization on the mixed cation sulfate (Ca, Na)SO$_4$

483   crystalline seeds, resulting in higher ERH values. On the other hand, in Cl-depleted ($X_{(Na,Mg)Cl} < 0.40$)

484   SSA particles, the first ERH values ranged from 46.0% to 24.6% as a random set of values higher than

485   the first ERHs in Na(Cl, NO$_3$) and (Na, Mg)(Cl, NO$_3$) mixture systems (Fig. 7), indicating

486   heterogeneous crystallization of the richer (Na, Mg)NO$_3$ moieties on the mixed cation sulfate

487   crystalline seeds for most particles.

488   The second/final ERH in the Na(Cl, NO$_3$) system was only observed for Cl-rich particles (X_{NaCl}

489   > 0.38) due to the mutual efflorescence of the eutonic component ($X_{NaCl} = 0.38$) at MERH =

490   ~30.0–35.5%, while no second ERH was recorded for Cl-depleted particles as NaNO$_3$ heterogeneously

491   crystallized simultaneously on the homogeneously nucleated NaCl seeds (Gupta et al., 2015a). For the

492   (Na, Mg)(Cl, NO$_3$), a second ERH = ~29.6–27.4% was only observed for $X_{(Na, Mg)Cl} = 0.5$ among the

493   three compositions measured (Fig. S3), probably due to the stochastic heterogeneous crystallization of

494   the Na(Cl, NO$_3$)-rich eutonic moiety on the NaCl seed. On the other hand, the typical transitions from

495   30.5% to 17.9% for the second/final ERH in ambient SSAs were only observed for Cl-depleted particles

496   with decreasing chloride concentration, i.e. $X_{(Na, Mg)Cl}$ = ~0.33 to 0.15, indicating homogeneous

497   nucleation of NaCl followed by assumed simultaneous heterogeneous crystallization of remaining

498   aqueous salt moieties such as Mg(SO$_4$, NO$_3$).

499   In the laboratory-generated (Na, Mg)(Cl, NO$_3$) particles with different mole fractions of

500   chloride, i.e. $X_{(Na, Mg)Cl}$ = 0.25, 0.5, 0.75 (Fig. S3), and 1.0 (Gupta et al., 2015a), clear final ERHs or

501   MERHs were observed at low RHs ranging in 11.0–5.1% ($X_{(Na, Mg)Cl}$ = 0.25, 0.5, and 1.0) and 14.6–12.1%

502   ($X_{(Na, Mg)Cl}$ = 0.75), probably due to the crystallization of the dominant eutonic component of

503   MgCl$_2$·4H$_2$O and MgCl$_2$·6H$_2$O, respectively. However, such low values of ERHs were not observed in

504   the ambient SSAs, possibly because the concentrations of MgCl$_2$·xH$_2$O were too small to be detected

505   by the optical microscopy-derived 2-D area ratio. On the other hand, the very gradual shrinkage

506   observed in ambient SSAs at low RHs may be due to the presence of amorphous Mg(NO$_3$, SO$_4$)·xH$_2$O

507   moieties, which were present in some particles (e.g., SSAs #5, #19, and #23 in Figs. 4a, 4d, and 5a).

508   Considering the possibility of water content at low RHs during the dehydration process (Cziczo

509   et al., 1997; Gupta et al., 2015a; Tang et al., 1997), the ambient SSAs can be divided into five potential

510   phases, denoted as alphabets (P, Q, R, S, T), based on the presence of different chemical components

511   and their states at different relative humidities (RHs) and the major chemical components in each phase

512   (s = solid; aq = aqueous) are listed as follows:

513   (i) P-(aq): Almost all components, including NaCl, NaNO$_3$, and Mg(Cl, NO$_3$, SO$_4$, organics), are

514   mixed in the aqueous phase at RH > ~55% for all mole fractions of chloride. The (Ca, Na)SO$_4$

515   should remain in the crystalline solid phase as it does not take part in the phase transitions within

516   the measured RH range.

517   (ii) Q-(s + aq): a mixed phase including solid NaCl and other heterogeneously crystallized moieties

518   + aqueous nucleating species like (Mg·xH$_2$O)$^{2+}$ and Cl$^-$/NO$_3^-$/SO$_4^{2-}$ at RHs < 50.5% in Cl-rich

519   SSAs ($X_{(Na, Mg)Cl}$ > 0.40).

520   (iii) R-(s + aq): a mixed phase including heterogeneously crystallized (Na, Mg)NO$_3$·xH$_2$O on

521   crystalline (Ca, Na)SO$_4$(xH$_2$O) seeds + aqueous NaCl and other moieties, between the first

522   ERHs = 46.0–24.6% and final ERHs = 30.5–17.9% for Cl-depleted SSAs ($X_{(Na, Mg)Cl}$ < 0.40).

523   (iv) S-(s + aq): a mixed phase including solid $(Na, Mg, Ca)(NO_3, SO_4) \cdot xH_2O$ and homogeneously

524   crystallized NaCl + aqueous/amorphous $(Mg \cdot xH_2O)^{2+}$ and NO_3^-/SO_4^{2-}, and other minor species

525   below final ERHs = 30.5–17.9% for Cl-depleted SSAs ($X_{(Na, Mg)Cl} < 0.40$).

526   (v) T-(s): All components are mixed in solid phase at RH = ~14.6–5.0% for all mole fractions of

527   chloride. Amorphous or gel forming $Mg(NO_3, SO_4) \cdot xH_2O$ shows gradual water loss, while only

528   a small amount of $MgCl_2 \cdot xH_2O$ is expected to crystallize.

529

530   **3.3 Non-SSA particles**

531   Generally, mineral particles such as aluminosilicates and calcium carbonate tend to be difficult

532   to absorb water and grow in size with increasing RH. However, these particles can become hygroscopic

533   after reaction with NO_x and SO_2 in the presence of water and/or mixing with SSAs. Particle #14 shown

534   in Fig. 8 is a highly aged aluminosilicate that has mixed with an SSA moiety, probably with $(Na, Mg)(Cl,$

535    $NO_3)$ and organic species as confirmed using X-ray spectrum. Clear deliquescence and efflorescence

536   transitions are observed in the gradual growth and shrinkage of particle #14 due mainly to the SSA part,

537   and the growth of the aged aluminosilicate is certainly smaller than the SSA at maximum RH. Particle

538   #20 shown in Fig. S6 is a reacted Ca-containing particle with nitrate showing gradual change in size

539   during humidification and dehydration processes, following hygroscopic property reported before (Ahn

540   et al., 2010). Particle #36 is a typical ammonium sulfate mixed with organic species as shown in Fig.

541   S7, and the major chemical components of particle #36 are C, N, O, and S. The particle showed a first

542   partial deliquescence transition at RH = 67.5%, which may be the MDRH for the mixture of ammonium

543   sulfate and organic species. Upon further increase in RH, the particle absorbed more moisture and fully

544   dissolved at RH = 77.1%, which is slightly lower than the DRH of pure ammonium sulfate particles

545   (Wu et al., 2019). During the dehydration process, particle #36 showed a slower rate of shrinkage than

546   ammonium sulfate particles, indicating inhibition of water evaporation due to surface hydrophobic

547   organic moieties, and effloresced at RH = 27.6%, which is lower than the ERH of ammonium sulfate

548   particles (Wu et al., 2019). Some particles, such as reacted Ca-containing particles #17 and #25 and an

549   aged SiO_2 particle #37, exhibit partial dissolution as shown in Fig. S8 and S9. The 2-D area ratio of

550   particle #17 at maximum RH is larger than that of particle #25, indicating the existence of more

551   hygroscopic components in particle #17. Particle #37 showed gradual increase and decrease with partial

552   dissolution only on the right side of particle, possibly due to the reacted Ca-containing one with nitrate

553   moiety. The observation of the hygroscopic behavior of particles having partial growth suggests that a

554 small content of hygroscopic chemical species can control the hygroscopic behavior of particles with
555 major non-hygroscopic species. On the other hand, genuine aluminosilicate particles #29 and #32 (Fig.
556 S10) and Fe-rich particles #2 and #7 (Fig. S11) did not show hygroscopic growth with changing RH.
557

4 Atmospheric Implications

559   The investigation of the hygroscopic behavior of ambient SSAs is crucial for understanding the
560 atmospheric chemistry and physics of marine environments. Previous studies have recognized that
561 SSAs contain a wide range of inorganic sea salt and organic species (Schiffer et al., 2018), making it
562 difficult to assess their hygroscopicity. In this study, the hygroscopic behavior of SSAs was
563 systematically characterized and correlated with the role of inorganic salt moieties and enriched organic
564 material coating. It was found that SSAs partially dissolve at lower RHs than the inorganic surrogates,
565 including $(Na, Mg)(Cl, NO_3)$, due to the coexistence with other soluble moieties such as water-soluble
566 secondary organics. This indicates that SSAs will be increasingly susceptible to trace gas species and
567 subsequent heterogeneous chemical reactions (Lee et al., 2020). The degree of chloride depletion was
568 also found to affect the hygroscopic behavior of aged SSAs. SSAs with a higher degree of chloride
569 depletion, i.e., higher aging degree, tend to exhibit multiple phase transitions with reducing RH,
570 retaining phase-separated core-shell mixing state, which impacts aerosol-radiation interactions (Sun et
571 al., 2018). The importance of considering these surrogate systems when modeling the hygroscopic
572 behavior of ambient SSAs is apparent, especially in the case of field observations where a wide range
573 of mixing states exist in particles. Even though there are still discrepancies regarding whether the
574 organic fraction can influence the hygroscopic growth of SSAs, this study demonstrated that organic
575 substances covering the sea salt moieties did suppress their hygroscopic growth. Further investigations,
576 including obtaining exact elemental and molecular compositions of the organic shells, are needed to
577 examine the aging of SSAs and quantify their uncertain effects on SSAs' hygroscopicity in
578 thermodynamic models.
579   In addition, other species involving mineral dust and anthropogenic particles can be transported
580 into marine environments and mixed with SSAs, which alter the particle compositions and in turn, their
581 hygroscopicity. Heterogeneous mixing or coating of SSAs onto less hygroscopic dust particles can
582 enhance their ability to interact with water vapor and reactive trace gases, leading to the formation of
583 new particles and increased CCN activity (Tang et al., 2016). This mixing can also affect the optical
584 properties and radiative forcing of atmospheric aerosols, as the scattering and absorption of solar

585 radiation by aerosols are dependent on their size, composition, and mixing state. Furthermore, the
586 impact of anthropogenic emissions on the hygroscopicity of marine aerosols is an important area of
587 research, as increased levels of atmospheric pollutants may enhance the aerosol-water interaction and
588 lead to changes in cloud properties and precipitation patterns (Su et al., 2022). Therefore, a
589 comprehensive understanding of the hygroscopic behavior of marine aerosols and their interactions
590 with other atmospheric constituents is necessary for accurately predicting their impacts on climate and
591 air quality.

592

5 Conclusions

594   The hygroscopic behavior of individual ambient aerosol particles collected at a coastal site of
595 Jeju Island, Korea, was investigated in correlation with their chemical compositions derived from X-
596 ray microanalysis. Specifically, we focused on the hygroscopic behavior of ambient aged SSAs and
597 their dependence on the extent of reaction between Cl^- and NO_3^- ions, estimated from the mixing ratios
598 of these ions using SEM-EDX. The phase transitions of the aged SSAs were found to be dominated by
599 inorganics involving $Na(Cl, NO_3)$ and/or $(Na, Mg)(Cl, NO_3)$ systems, with organic surfactant films
600 covering the droplets suppressing hygroscopic growth and shrinkage with changing RH. For Cl-rich
601 SSAs, two major transitions were observed during the humidification process, firstly at the MDRH and
602 secondly at a final DRH. During the dehydration process, Cl-rich SSAs showed single-stage
603 efflorescence. Cl-depleted SSAs showed two prompt deliquescence transitions during the
604 humidification process and stepwise transitions during the dehydration process, depending on their
605 chemical compositions.

606   The hygroscopic behavior of other particle types, including aged aluminosilicate, Ca-containing,
607 organic and ammonium sulfate mixture, and Fe-rich particles, was also observed. Aged mineral
608 particles showed varying degrees of size changes with changing RH, potentially due to the presence of
609 SSAs and/or NO_3^- species resulting from coagulation and heterogeneous reactions, while non-reacted
610 mineral and Fe-rich particles did not exhibit significant size changes during the hygroscopic process.
611 The mixture particles of organic and ammonium sulfate displayed lower DRH and ERH values
612 compared to pure ammonium sulfate salt, indicating the impact of organic species on the hygroscopic
613 behavior of ammonium sulfate. While there have been some studies on the hygroscopic behavior of
614 ambient marine aerosols, this study is one of the first to systematically investigate their hygroscopic

615 behavior and to correlate it with their chemical compositions, providing better insights into their impact

616 on climate change and atmospheric chemistry.

617

618 **Data availability**

619 The data used in this study are available upon request; please contact Chul-Un Ro (curo@inha.ac.kr).

620

621 **Author contributions**

622 LW, HJE, HY, DG, and HRC designed the experiment. LW, HJE, HY, and HRC carried out the

623 measurements and/or analyzed the data. LW, HJE, HY, DG, HRC, PF, and CUR contributed discussion

624 of the data. LW, HJE, DG, and CUR drafted the paper.

625

626 **Competing interests**

627 The authors declare that they have no conflict of interest.

628

629 **Acknowledgements**

630 This study was supported by the National Research Foundation of Korea (NRF) grant funded by the

631 Korean government (MSIT) (No. 2021R1A4A1032579 and No. 2021R1A2C2004240) and by the

632 National Institute of Environmental Research (NIER) funded by the Ministry of Environment (MOE)

633 of Korea (NIER-2021-03-03-007).

634

635 **References**

636 Ahn, K.-H., Kim, S.-M., Jung, H.-J., Lee, M.-J., Eom, H.-J., Maskey, S., and Ro, C.-U.: Combined Use
637   of Optical and Electron Microscopic Techniques for the Measurement of Hygroscopic Property,
638   Chemical Composition, and Morphology of Individual Aerosol Particles, Anal. Chem., 82, 7999-
639   8009, 10.1021/ac101432y, 2010.

640 Ansari, A. S. and Pandis, S. N.: Prediction of multicomponent inorganic atmospheric aerosol behavior,
641   Atmos. Environ., 33, 745-757, http://dx.doi.org/10.1016/S1352-2310(98)00221-0, 1999.

642 Atkinson, D. B., Radney, J. G., Lum, J., Kolesar, K. R., Cziczo, D. J., Pekour, M. S., Zhang, Q., Setyan,
643   A., Zelenyuk, A., and Cappa, C. D.: Aerosol optical hygroscopicity measurements during the 2010
644   CARES campaign, Atmos. Chem. Phys, 15, 4045-4061, 10.5194/acp-15-4045-2015, 2015.

645 Ault, A. P., Guasco, T. L., Baltrusaitis, J., Ryder, O. S., Trueblood, J. V., Collins, D. B., Ruppel, M. J.,
646   Cuadra-Rodriguez, L. A., Prather, K. A., and Grassian, V. H.: Heterogeneous Reactivity of Nitric
647   Acid with Nascent Sea Spray Aerosol: Large Differences Observed between and within Individual
648   Particles, J. Phys. Chem. Lett, 5, 2493-2500, 10.1021/jz5008802, 2014.

649 Ault, A. P., Moffet, R. C., Baltrusaitis, J., Collins, D. B., Ruppel, M. J., Cuadra-Rodriguez, L. A., Zhao,
650   D., Guasco, T. L., Ebben, C. J., Geiger, F. M., Bertram, T. H., Prather, K. A., and Grassian, V. H.:

Size-Dependent Changes in Sea Spray Aerosol Composition and Properties with Different Seawater Conditions, Environ. Sci. Technol., 47, 5603-5612, 10.1021/es400416g, 2013.

Beardsley, R., Jang, M., Ori, B., Im, Y., Delcomyn, C. A., and Witherspoon, N.: Role of sea salt aerosols in the formation of aromatic secondary organic aerosol: yields and hygroscopic properties, Environ. Chem., 10, 167-177, http://dx.doi.org/10.1071/EN13016, 2013.

Bertram, T. H., Cochran, R. E., Grassian, V. H., and Stone, E. A.: Sea spray aerosol chemical composition: elemental and molecular mimics for laboratory studies of heterogeneous and multiphase reactions, Chem. Soc. Rev., 47, 2374-2400, 10.1039/c7cs00008a, 2018.

Carslaw, K. S., Clegg, S. L., and Brimblecombe, P.: A Thermodynamic Model of the System HCl-HNO3-H2SO4-H2O, Including Solubilities of HBr, from < 200 to 328 K, J. Phys. Chem. A, 99, 11557-11574, 10.1021/j100029a039, 1995.

Chan, C. K., Ha, Z., and Choi, M. Y.: Study of water activities of aerosols of mixtures of sodium and magnesium salts, Atmos. Environ., 34, 4795-4803, 10.1016/S1352-2310(00)00252-1, 2000.

Chan, C. K., Liang, Z., Zheng, J., Clegg, S. L., and Brimblecombe, P.: Thermodynamic properties of aqueous aerosols to high supersaturation: I—measurements of water activity of the system $Na^+-Cl^--NO_3^--SO_4^{2-}-H_2O$ at~ 298.15 K, Aerosol Sci. Technol., 27, 324-344, 10.1080/02786829708965477, 1997.

Chang, S.-Y. and Lee, C.-T.: Applying GC-TCD to investigate the hygroscopic characteristics of mixed aerosols, Atmos. Environ., 36, 1521-1530, 10.1016/S1352-2310(01)00546-5, 2002.

Clegg, S. L., Brimblecombe, P., and Wexler, A. S.: Thermodynamic Model of the System $H^+-NH_4^+-Na^+-SO_4^{2-}-NO_3^--Cl^--H_2O$ at 298.15 K, J. Phys. Chem. A, 102, 2155-2171, 10.1021/jp973043j, 1998a.

Clegg, S. L., Brimblecombe, P., and Wexler, A. S.: Thermodynamic Model of the System $H^+-NH_4^+-SO_4^{2-}-NO_3^--H_2O$ at Tropospheric Temperatures, J. Phys. Chem. A, 102, 2137-2154, 10.1021/jp973042r, 1998b.

Cochran, R. E., Laskina, O., Jayarathne, T., Laskin, A., Laskin, J., Lin, P., Sultana, C., Lee, C., Moore, K. A., Cappa, C. D., Bertram, T. H., Prather, K. A., Grassian, V. H., and Stone, E. A.: Analysis of Organic Anionic Surfactants in Fine and Coarse Fractions of Freshly Emitted Sea Spray Aerosol, Environ. Sci. Technol., 50, 2477-2486, 10.1021/acs.est.5b04053, 2016.

Cochran, R. E., Laskina, O., Trueblood, J. V., Estillore, A. D., Morris, H. S., Jayarathne, T., Sultana, C. M., Lee, C., Lin, P., Laskin, J., Laskin, A., Dowling, J. A., Qin, Z., Cappa, C. D., Bertram, T. H., Tivanski, A. V., Stone, E. A., Prather, K. A., and Grassian, V. H.: Molecular Diversity of Sea Spray Aerosol Particles: Impact of Ocean Biology on Particle Composition and Hygroscopicity, Chem, 2, 655-667, 10.1016/j.chempr.2017.03.007, 2017.

Cohen, M. D., Flagan, R. C., and Seinfeld, J. H.: Studies of concentrated electrolyte solutions using the electrodynamic balance. 3. Solute nucleation, J. Phys. Chem, 91, 4583-4590, 10.1021/j100301a031, 1987.

Cziczo, D. J., Nowak, J. B., Hu, J. H., and Abbatt, J. P. D.: Infrared spectroscopy of model tropospheric aerosols as a function of relative humidity: Observation of deliquescence and crystallization, J. Geophys. Res. Atmos., 102, 18843-18850, 10.1029/97jd01361, 1997.

Eom, H.-J., Gupta, D., Li, X., Jung, H.-J., Kim, H., and Ro, C.-U.: Influence of Collecting Substrates on the Characterization of Hygroscopic Properties of Inorganic Aerosol Particles, Anal. Chem., 86, 2648-2656, 10.1021/ac4042075, 2014.

Eom, H. J., Gupta, D., Cho, H. R., Hwang, H., Hur, S., Gim, Y., and Ro, C. U.: Single-particle investigation of summertime and wintertime Antarctic sea spray aerosols using low-Z particle

696   EPMA, Raman microspectrometry, and ATR-FTIR imaging techniques, Atmos. Chem. Phys.,
697   2016, 1-30, 10.5194/acp-2016-584, 2016.
698   Finlayson-Pitts, B. J. and Pitts, J. N.: Chemistry of the upper and lower atmosphere : theory,
699   experiments, and applications, Academic Press, San Diego, 2000.
700   Forestieri, S. D., Cornwell, G. C., Helgestad, T. M., Moore, K. A., Lee, C., Novak, G. A., Sultana, C.
701   M., Wang, X., Bertram, T. H., Prather, K. A., and Cappa, C. D.: Linking variations in sea spray
702   aerosol particle hygroscopicity to composition during two microcosm experiments, Atmos. Chem.
703   Phys., 16, 9003-9018, 10.5194/acp-16-9003-2016, 2016.
704   Freney, E. J., Adachi, K., and Buseck, P. R.: Internally mixed atmospheric aerosol particles:
705   Hygroscopic growth and light scattering, J. Geophys. Res. Atmos., 115, D19210,
706   10.1029/2009jd013558, 2010.
707   Gard, E. E., Kleeman, M. J., Gross, D. S., Hughes, L. S., Allen, J. O., Morrical, B. D., Fergenson, D.
708   P., Dienes, T., E. Gälli, M., and Johnson, R. J.: Direct observation of heterogeneous chemistry in
709   the atmosphere, Science, 279, 1184-1187, 10.1126/science.279.5354.1184, 1998.
710   Ge, Z., Wexler, A. S., and Johnston, M. V.: Multicomponent Aerosol Crystallization, J. Colloid Interface
711   Sci., 183, 68-77, http://dx.doi.org/10.1006/jcis.1996.0519, 1996.
712   Ge, Z., Wexler, A. S., and Johnston, M. V.: Deliquescence Behavior of Multicomponent Aerosols, J.
713   Phys. Chem. A, 102, 173-180, 10.1021/jp972396f, 1998.
714   Geng, H., Hwang, H., Liu, X., Dong, S., and Ro, C. U.: Investigation of aged aerosols in size-resolved
715   Asian dust storm particles transported from Beijing, China, to Incheon, Korea, using low-Z
716   particle EPMA, Atmos. Chem. Phys., 14, 3307-3323, 10.5194/acp-14-3307-2014, 2014.
717   Geng, H., Kang, S., Jung, H. J., Choël, M., Kim, H., and Ro, C. U.: Characterization of individual
718   submicrometer aerosol particles collected in Incheon, Korea, by quantitative transmission electron
719   microscopy energy-dispersive X-ray spectrometry, J. Geophys. Res. Atmos., 115,
720   10.1029/2009JD013486, 2010.
721   Ghorai, S., Wang, B., Tivanski, A., and Laskin, A.: Hygroscopic properties of internally mixed particles
722   composed of NaCl and water-soluble organic acids, Environ. Sci. Technol., 48, 2234-2241,
723   10.1021/es404727u, 2014.
724   Guo, L., Gu, W., Peng, C., Wang, W., Li, Y. J., Zong, T., Tang, Y., Wu, Z., Lin, Q., Ge, M., Zhang, G.,
725   Hu, M., Bi, X., Wang, X., and Tang, M.: A comprehensive study of hygroscopic properties of
726   calcium- and magnesium-containing salts: implication for hygroscopicity of mineral dust and sea
727   salt aerosols, Atmos. Chem. Phys, 19, 2115-2133, 10.5194/acp-19-2115-2019, 2019.
728   Gupta, D., Eom, H. J., Cho, H. R., and Ro, C. U.: Hygroscopic behavior of NaCl–MgCl$_2$ mixture
729   particles as nascent sea-spray aerosol surrogates and observation of efflorescence during
730   humidification, Atmos. Chem. Phys., 15, 11273-11290, 10.5194/acp-15-11273-2015, 2015a.
731   Gupta, D., Kim, H., Park, G., Li, X., Eom, H. J., and Ro, C. U.: Hygroscopic properties of NaCl and
732   NaNO$_3$ mixture particles as reacted inorganic sea-salt aerosol surrogates, Atmos. Chem. Phys., 15,
733   3379-3393, 10.5194/acp-15-3379-2015, 2015b.
734   Haynes, W. M.: CRC Handbook of Chemistry and Physics, 96th Edition, CRC Press, Boca Raton,
735   Florida, 14–18, 2015.
736   Haywood, J. and Boucher, O.: Estimates of the direct and indirect radiative forcing due to tropospheric
737   aerosols: A review, Rev. Geophys., 38, 513-543, 10.1029/1999rg000078, 2000.
738   Herich, H., Kammermann, L., Friedman, B., Gross, D. S., Weingartner, E., Lohmann, U., Spichtinger,
739   P., Gysel, M., Baltensperger, U., and Cziczo, D. J.: Subarctic atmospheric aerosol composition: 2.
740   Hygroscopic growth properties, J. Geophys. Res. Atmos., 114, D13204, 10.1029/2008jd011574,
741   2009.

Keene, W. C., Maring, H., Maben, J. R., Kieber, D. J., Pszenny, A. A. P., Dahl, E. E., Izaguirre, M. A., Davis, A. J., Long, M. S., Zhou, X., Smoydzin, L., and Sander, R.: Chemical and physical characteristics of nascent aerosols produced by bursting bubbles at a model air-sea interface, J. Geophys. Res. Atmos., 112, D21202, 10.1029/2007jd008464, 2007.

Kim, H., Lee, M.-J., Jung, H.-J., Eom, H.-J., Maskey, S., Ahn, K.-H., and Ro, C.-U.: Hygroscopic behavior of wet dispersed and dry deposited NaNO3 particles, Atmos. Environ., 60, 68-75, http://dx.doi.org/10.1016/j.atmosenv.2012.06.011, 2012.

Kong, X., Wolf, M. J., Roesch, M., Thomson, E. S., Bartels-Rausch, T., Alpert, P. A., Ammann, M., Prisle, N. L., and Cziczo, D. J.: A continuous flow diffusion chamber study of sea salt particles acting as cloud nuclei: deliquescence and ice nucleation, Tellus B: Chem. Phys. Meteorol., 70, 1-11, 10.1080/16000889.2018.1463806, 2018.

Krieger, U. K., Marcolli, C., and Reid, J. P.: Exploring the complexity of aerosol particle properties and processes using single particle techniques, Chem. Soc. Rev., 41, 6631-6662, 10.1039/c2cs35082c, 2012.

Krueger, B. J., Grassian, V. H., Iedema, M. J., Cowin, J. P., and Laskin, A.: Probing Heterogeneous Chemistry of Individual Atmospheric Particles Using Scanning Electron Microscopy and Energy-Dispersive X-ray Analysis, Anal. Chem., 75, 5170-5179, 10.1021/ac034455t, 2003.

Laskin, A., Moffet, R. C., Gilles, M. K., Fast, J. D., Zaveri, R. A., Wang, B., Nigge, P., and Shutthanandan, J.: Tropospheric chemistry of internally mixed sea salt and organic particles: Surprising reactivity of NaCl with weak organic acids, J. Geophys. Res. Atmos., 117, Tropospheric chemistry of internally mixed sea salt and organic particles: Surprising reactivity of NaCl with weak organic acids, 2012.

Lee, H. D., Morris, H. S., Laskina, O., Sultana, C. M., Lee, C., Jayarathne, T., Cox, J. L., Wang, X., Hasenecz, E. S., DeMott, P. J., Bertram, T. H., Cappa, C. D., Stone, E. A., Prather, K. A., Grassian, V. H., and Tivanski, A. V.: Organic Enrichment, Physical Phase State, and Surface Tension Depression of Nascent Core–Shell Sea Spray Aerosols during Two Phytoplankton Blooms, ACS Earth Space Chem., 4, 650-660, 10.1021/acsearthspacechem.0c00032, 2020.

Li, X., Wu, L., Lee, J.-S., and Ro, C.-U.: Hygroscopic behavior and chemical reactivity of aerosols generated from mixture solutions of low molecular weight dicarboxylic acids and NaCl, Phys. Chem. Chem. Phys., 23, 11052-11064, 10.1039/d1cp00590a, 2021.

Li, X., Gupta, D., Eom, H.-J., Kim, H., and Ro, C.-U.: Deliquescence and efflorescence behavior of individual NaCl and KCl mixture aerosol particles, Atmos. Environ., 82, 36-43, http://dx.doi.org/10.1016/j.atmosenv.2013.10.011, 2014.

Li, Y. J., Liu, P. F., Bergoend, C., Bateman, A. P., and Martin, S. T.: Rebounding hygroscopic inorganic aerosol particles: Liquids, gels, and hydrates, Aerosol Sci. Technol., 51, 388-396, 10.1080/02786826.2016.1263384, 2016.

Liu, Y. and Laskin, A.: Hygroscopic Properties of CH3SO3Na, CH3SO3NH4, (CH3SO3)2Mg, and (CH3SO3)2Ca Particles Studied by micro-FTIR Spectroscopy, J. Phys. Chem. A, 113, 1531-1538, 10.1021/jp8079149, 2009.

Liu, Y., Cain, J. P., Wang, H., and Laskin, A.: Kinetic Study of Heterogeneous Reaction of Deliquesced NaCl Particles with Gaseous HNO3 Using Particle-on-Substrate Stagnation Flow Reactor Approach, J. Phys. Chem. A, 111, 10026-10043, 10.1021/jp072005p, 2007.

Liu, Y., Minofar, B., Desyaterik, Y., Dames, E., Zhu, Z., Cain, J. P., Hopkins, R. J., Gilles, M. K., Wang, H., and Jungwirth, P.: Internal structure, hygroscopic and reactive properties of mixed sodium methanesulfonate-sodium chloride particles, Phys. Chem. Chem. Phys., 13, 11846-11857, 10.1039/C1CP20444K, 2011.

788 Martin, S. T.: Phase Transitions of Aqueous Atmospheric Particles, Chem. Rev., 100, 3403-3454,
789   10.1021/cr990034t, 2000.
790 Meskhidze, N., Petters, M. D., Tsigaridis, K., Bates, T., O'Dowd, C., Reid, J., Lewis, E. R., Gantt, B.,
791   Anguelova, M. D., Bhave, P. V., Bird, J., Callaghan, A. H., Ceburnis, D., Chang, R., Clarke, A.,
792   de Leeuw, G., Deane, G., DeMott, P. J., Elliot, S., Facchini, M. C., Fairall, C. W., Hawkins, L.,
793   Hu, Y., Hudson, J. G., Johnson, M. S., Kaku, K. C., Keene, W. C., Kieber, D. J., Long, M. S.,
794   Mårtensson, M., Modini, R. L., Osburn, C. L., Prather, K. A., Pszenny, A., Rinaldi, M., Russell, L.
795   M., Salter, M., Sayer, A. M., Smirnov, A., Suda, S. R., Toth, T. D., Worsnop, D. R., Wozniak, A.,
796   and Zorn, S. R.: Production mechanisms, number concentration, size distribution, chemical
797   composition, and optical properties of sea spray aerosols, Atmos. Sci. Lett., 14, 207-213,
798   10.1002/asl2.441, 2013.
799 Mikhailov, E., Vlasenko, S., Martin, S. T., Koop, T., and Pöschl, U.: Amorphous and crystalline aerosol
800   particles interacting with water vapor: conceptual framework and experimental evidence for
801   restructuring, phase transitions and kinetic limitations, Atmos. Chem. Phys, 9, 9491-9522,
802   10.5194/acp-9-9491-2009, 2009.
803 Ming, Y. and Russell, L. M.: Predicted hygroscopic growth of sea salt aerosol, J. Geophys. Res. Atmos.,
804   106, 28259-28274, 10.1029/2001jd000454, 2001.
805 Nguyen, Q. T., Kjær, K. H., Kling, K. I., Boesen, T., and Bilde, M.: Impact of fatty acid coating on the
806   CCN activity of sea salt particles, Tellus B: Chem. Phys. Meteorol., 69, 1304064,
807   10.1080/16000889.2017.1304064, 2017.
808 Niedermeier, D., Wex, H., Voigtländer, J., Stratmann, F., Brüggemann, E., Kiselev, A., Henk, H., and
809   Heintzenberg, J.: LACIS-measurements and parameterization of sea-salt particle hygroscopic
810   growth and activation, Atmos. Chem. Phys., 8, 579-590, 10.5194/acp-8-579-2008, 2008.
811 O'Dowd, C. D. and de Leeuw, G.: Marine aerosol production: a review of the current knowledge, Philos.
812   trans., Math. phys. eng. sci., 365, 1753-1774, 10.1098/rsta.2007.2043, 2007.
813 Pandis, S. N., Wexler, A. S., and Seinfeld, J. H.: Dynamics of Tropospheric Aerosols, J. Phys. Chem.,
814   99, 9646-9659, 10.1021/j100024a003, 1995.
815 Pöschl, U. and Shiraiwa, M.: Multiphase Chemistry at the Atmosphere–Biosphere Interface Influencing
816   Climate and Public Health in the Anthropocene, Chem. Rev., 115, 4440-4475, 10.1021/cr500487s,
817   2015.
818 Pósfai, M., Anderson, J. R., Buseck, P. R., and Sievering, H.: Compositional variations of sea-salt-mode
819   aerosol particles from the North Atlantic, J. Geophys. Res. Atmos., 100, 23063-23074,
820   10.1029/95jd01636, 1995.
821 Prather, K. A., Bertram, T. H., Grassian, V. H., Deane, G. B., Stokes, M. D., DeMott, P. J., Aluwihare,
822   L. I., Palenik, B. P., Azam, F., Seinfeld, J. H., Moffet, R. C., Molina, M. J., Cappa, C. D., Geiger,
823   F. M., Roberts, G. C., Russell, L. M., Ault, A. P., Baltrusaitis, J., Collins, D. B., Corrigan, C. E.,
824   Cuadra-Rodriguez, L. A., Ebben, C. J., Forestieri, S. D., Guasco, T. L., Hersey, S. P., Kim, M. J.,
825   Lambert, W. F., Modini, R. L., Mui, W., Pedler, B. E., Ruppel, M. J., Ryder, O. S., Schoepp, N. G.,
826   Sullivan, R. C., and Zhao, D.: Bringing the ocean into the laboratory to probe the chemical
827   complexity of sea spray aerosol, Proc. Natl. Acad. Sci. USA, 110, 7550-7555,
828   10.1073/pnas.1300262110, 2013.
829 Quinn, P. K., Collins, D. B., Grassian, V. H., Prather, K. A., and Bates, T. S.: Chemistry and Related
830   Properties of Freshly Emitted Sea Spray Aerosol, Chem. Rev., 10.1021/cr500713g, 2015.
831 Rosati, B., Christiansen, S., Dinesen, A., Roldin, P., Massling, A., Nilsson, E. D., and Bilde, M.: The
832   impact of atmospheric oxidation on hygroscopicity and cloud droplet activation of inorganic sea
833   spray aerosol, Sci. Rep., 11, 10008, 10.1038/s41598-021-89346-6, 2021.

834 Ryder, O. S., Ault, A. P., Cahill, J. F., Guasco, T. L., Riedel, T. P., Cuadra-Rodriguez, L. A., Gaston, C.
835   J., Fitzgerald, E., Lee, C., Prather, K. A., and Bertram, T. H.: On the Role of Particle Inorganic
836   Mixing State in the Reactive Uptake of N_2O_5 to Ambient Aerosol Particles, Environ. Sci. Technol.,
837   48, 1618-1627, 10.1021/es4042622, 2014.
838 Saul, T. D., Tolocka, M. P., and Johnston, M. V.: Reactive Uptake of Nitric Acid onto Sodium Chloride
839   Aerosols Across a Wide Range of Relative Humidities, J. Phys. Chem. A, 110, 7614-7620,
840   10.1021/jp060639a, 2006.
841 Schiffer, J. M., Mael, L. E., Prather, K. A., Amaro, R. E., and Grassian, V. H.: Sea Spray Aerosol: Where
842   Marine Biology Meets Atmospheric Chemistry, ACS Cent. Sci., 4, 1617-1623,
843   10.1021/acscentsci.8b00674, 2018.
844 Schill, S. R., Collins, D. B., Lee, C., Morris, H. S., Novak, G. A., Prather, K. A., Quinn, P. K., Sultana,
845   C. M., Tivanski, A. V., Zimmermann, K., Cappa, C. D., and Bertram, T. H.: The Impact of Aerosol
846   Particle Mixing State on the Hygroscopicity of Sea Spray Aerosol, ACS Cent. Sci., 1, 132-141,
847   10.1021/acscentsci.5b00174, 2015.
848 Schindelholz, E., Risteen, B., and Kelly, R.: Effect of relative humidity on corrosion of steel under sea
849   salt aerosol proxies: I. NaCl, J. Electrochem. Soc., 161, C450, 10.1149/2.0221410jes, 2014.
850 Seinfeld, J. H. and Pandis, S. N.: Atmospheric chemistry and physics: from air pollution to climate
851   change, 2nd ed., J. Wiley, Hoboken NJ, 1203 pp., 2006.
852 Semeniuk, T. A., Wise, M. E., Martin, S. T., Russell, L. M., and Buseck, P. R.: Water uptake
853   characteristics of individual atmospheric particles having coatings, Atmos. Environ., 41, 6225-
854   6235, 10.1016/j.atmosenv.2007.04.001, 2007.
855 Song, Y., Li, J., Tsona, N. T., Liu, L., and Du, L.: Enrichment of short-chain organic acids transferred
856   to submicron sea spray aerosols, Sci. Total Environ., 851, 158122,
857   10.1016/j.scitotenv.2022.158122, 2022.
858 Su, B., Wang, T., Zhang, G., Liang, Y., Lv, C., Hu, Y., Li, L., Zhou, Z., Wang, X., and Bi, X.: A review
859   of atmospheric aging of sea spray aerosols: Potential factors affecting chloride depletion, Atmos.
860   Environ., 290, 10.1016/j.atmosenv.2022.119365, 2022.
861 Sun, J., Liu, L., Xu, L., Wang, Y., Wu, Z., Hu, M., Shi, Z., Li, Y., Zhang, X., Chen, J., and Li W.,: Key
862   role of nitrate in phase transitions of urban particles: implications of important reactive surfaces
863   for secondary aerosol formation, J. Geophys. Res. Atmos., 123, 1234-1243,
864   10.1002/2017JD027264, 2018.
865 Tang, I. N., Tridico, A. C., and Fung, K. H.: Thermodynamic and optical properties of sea salt aerosols,
866   J. Geophys. Res. Atmos., 102, 23269-23275, 10.1029/97jd01806, 1997.
867 Tang, M., Cziczo, D. J., and Grassian, V. H.: Interactions of water with mineral dust aerosol: water
868   adsorption, hygroscopicity, cloud condensation, and ice nucleation, Chem. Rev., 116, 4205-4259,
869   10.1021/acs.chemrev.5b00529, 2016.
870 ten Brink, H. M.: Reactive uptake of HNO_3 and H_2SO_4 in sea-salt (NaCl) particles, J. Aerosol Sci., 29,
871   57-64, http://dx.doi.org/10.1016/S0021-8502(97)00460-6, 1998.
872 Tobon, Y. A., El Hajj, D., Seng, S., Bengrad, F., Moreau, M., Visez, N., Chiapello, I., Crumeyrolle, S.,
873   and Choel, M.: Impact of the particle mixing state on the hygroscopicity of internally mixed
874   sodium chloride-ammonium sulfate single droplets: a theoretical and experimental study, Phys.
875   Chem. Chem. Phys., 23, 14391-14403, 10.1039/d1cp01574e, 2021.
876 Vaishya, A., Ovadnevaite, J., Bialek, J., Jennings, S. G., Ceburnis, D., and O'Dowd, C. D.: Bistable
877   effect of organic enrichment on sea spray radiative properties, Geophys. Res. Lett., 40, 6395-6398,
878   10.1002/2013gl058452, 2013.

879 Vekemans, B., Janssens, K., Vincze, L., Adams, F., and Van Espen, P.: Analysis of X-ray spectra by
880   iterative least squares (AXIL): New developments, Xray Spectrom., 23, 278-285,
881   10.1002/xrs.1300230609, 1994.
882 Wang, J. and Martin, S. T.: Satellite characterization of urban aerosols: Importance of including
883   hygroscopicity and mixing state in the retrieval algorithms, J. Geophys. Res. Atmos., 112, D17203,
884   10.1029/2006jd008078, 2007.
885 Wang, X., Sultana, C. M., Trueblood, J., Hill, T. C., Malfatti, F., Lee, C., Laskina, O., Moore, K. A.,
886   Beall, C. M., and McCluskey, C. S.: Microbial control of sea spray aerosol composition: A tale of
887   two blooms, ACS Central Science, 1, 124-131, 10.1021/acscentsci.5b00148, 2015.
888 Wang, X., Deane, G. B., Moore, K. A., Ryder, O. S., Stokes, M. D., Beall, C. M., Collins, D. B.,
889   Santander, M. V., Burrows, S. M., Sultana, C. M., and Prather, K. A.: The role of jet and film drops
890   in controlling the mixing state of submicron sea spray aerosol particles, Proc. Natl. Acad. Sci.
891   USA, 114, 6978-6983, 10.1073/pnas.1702420114, 2017.
892 Wexler, A. S. and Clegg, S. L.: Atmospheric aerosol models for systems including the ions H^+, NH_4^+,
893   Na^+, SO_4^{2-}, NO_3^-, Cl^-, Br^-, and H_2O, J. Geophys. Res. A, 107, D14, 4207, 10.1029/2001jd000451,
894   2002.
895 Wexler, A. S. and Seinfeld, J. H.: Second-generation inorganic aerosol model, Atmos. Environ., 27A,
896   25, 2731-2748, 10.1016/0960-1686(91)90203-J, 1991.
897 Wise, M. E., Semeniuk, T. A., Bruintjes, R., Martin, S. T., Russell, L. M., and Buseck, P. R.:
898   Hygroscopic behavior of NaCl-bearing natural aerosol particles using environmental transmission
899   electron microscopy, J. Geophys. Res. Atmos., 112, D10224, 10.1029/2006jd007678, 2007.
900 Wise, M. E., Freney, E. J., Tyree, C. A., Allen, J. O., Martin, S. T., Russell, L. M., and Buseck, P. R.:
901   Hygroscopic behavior and liquid-layer composition of aerosol particles generated from natural
902   and artificial seawater, J. Geophys. Res. Atmos., 114, D03201, 10.1029/2008jd010449, 2009.
903 Woods, E., Chung, D., Lanney, H. M., and Ashwell, B. A.: Surface Morphology and Phase Transitions
904   in Mixed NaCl/MgSO4 Aerosol Particles, J. Phys. Chem. A, 114, 2837-2844, 10.1021/jp911133j,
905   2010.
906 Woods, E., Heylman, K. D., Gibson, A. K., Ashwell, A. P., and Rossi, S. R.: Effects of NOy Aging on
907   the Dehydration Dynamics of Model Sea Spray Aerosol, J. Phys. Chem. A, 117, 4214-4222,
908   10.1021/jp401646d, 2013.
909 Wu, L., Li, X., and Ro, C.-U.: Hygroscopic Behavior of Ammonium Sulfate, Ammonium Nitrate, and
910   their Mixture Particles, Asian J. Atmos., 13, 196-211, 10.5572/ajae.2019.13.3.196, 2019.
911 Wu, L., Becote, C., Sobanska, S., Flaud, P.-M., Perraudin, E., Villenave, E., Song, Y.-C., and Ro, C.-
912   U.: Hygroscopic behavior of aerosols generated from solutions of 3-methyl-1,2,3-
913   butanetricarboxylic acid, its sodium salts, and its mixtures with NaCl, Atmos. Chem. Phys., 20,
914   14103-14122, 10.5194/acp-20-14103-2020, 2020.
915 Xiao, H.-S., Dong, J.-L., Wang, L.-Y., Zhao, L.-J., Wang, F., and Zhang, Y.-H.: Spatially resolved
916   micro-raman observation on the phase separation of effloresced sea salt droplets, Environ. Sci.
917   Technol., 42, 8698-8702, 10.1021/es801181f, 2008.
918 Xu, W., Ovadnevaite, J., Fossum, K. N., Lin, C., Huang, R.-J., O'Dowd, C., and Ceburnis, D.: Aerosol
919   hygroscopicity and its link to chemical composition in the coastal atmosphere of Mace Head:
920   marine and continental air masses, Atmos. Chem. Phys, 20, 3777-3791, 10.5194/acp-20-3777-
921   2020, 2020.
922 Zhang, X., Massoli, P., Quinn, P. K., Bates, T. S., and Cappa, C. D.: Hygroscopic growth of submicron
923   and supermicron aerosols in the marine boundary layer, J. Geophys. Res. Atmos., 119, 8384-8399,
924   10.1002/2013jd021213, 2014.

925 Zhang, Y.-H., Choi, M. Y., and Chan, C. K.: Relating Hygroscopic Properties of Magnesium Nitrate to
926   the Formation of Contact Ion Pairs, J. Phys. Chem. A, 108, 1712-1718, 10.1021/jp036524d, 2004.
927 Zhao, L.-J., Zhang, Y.-H., Wei, Z.-F., Cheng, H., and Li, X.-H.: Magnesium Sulfate Aerosols Studied
928   by FTIR Spectroscopy: Hygroscopic Properties, Supersaturated Structures, and Implications for
929   Seawater Aerosols, J. Phys. Chem. A, 110, 951-958, 10.1021/jp055291i, 2006.
930 Zieger, P., Vaisanen, O., Corbin, J. C., Partridge, D. G., Bastelberger, S., Mousavi-Fard, M., Rosati, B.,
931   Gysel, M., Krieger, U. K., Leck, C., Nenes, A., Riipinen, I., Virtanen, A., and Salter, M. E.:
932   Revising the hygroscopicity of inorganic sea salt particles, Nat. Commun., 8, 15883,
933   10.1038/ncomms15883, 2017.
934 Zuend, A., Marcolli, C., Luo, B. P., and Peter, T.: A thermodynamic model of mixed organic-inorganic
935   aerosols to predict activity coefficients, Atmos. Chem. Phys., 8, 4559–4593, 10.5194/acp-8-4559-
936   2008, 2008.
937 Zuend, A., Marcolli, C., Booth, A. M., Lienhard, D. M., Soonsin, V., Krieger, U. K., Topping, D. O.,
938   McFiggans, G., Peter, T., and Seinfeld, J. H.: New and extended parameterization of the
939   thermodynamic model AIOMFAC: calculation of activity coefficients for organic-inorganic
940   mixtures containing carboxyl, hydroxyl, carbonyl, ether, ester, alkenyl, alkyl, and aromatic
941   functional groups, Atmos. Chem. Phys., 11, 9155–9206, 10.5194/acp-11-9155-2011, 2011.

942

943 **Figure 1.** Location of Gosan sampling site on Jeju Island, South Korea. (Map Copyright © Google Earth)

944

945

946 **Figure 2.** (a) Secondary electron image (SEI) of the first field containing 16 particles and X-ray spectra of (b) a Cl-rich and (c) a Cl-
947 depleted aged SSAs **(**particles #5 and #11, respectively**).** In this image, aged SSAs, Fe-containing particles, and aluminosilicates are
948 denoted as "r-SS", "Fe-rich", and "AlSi", respectively.
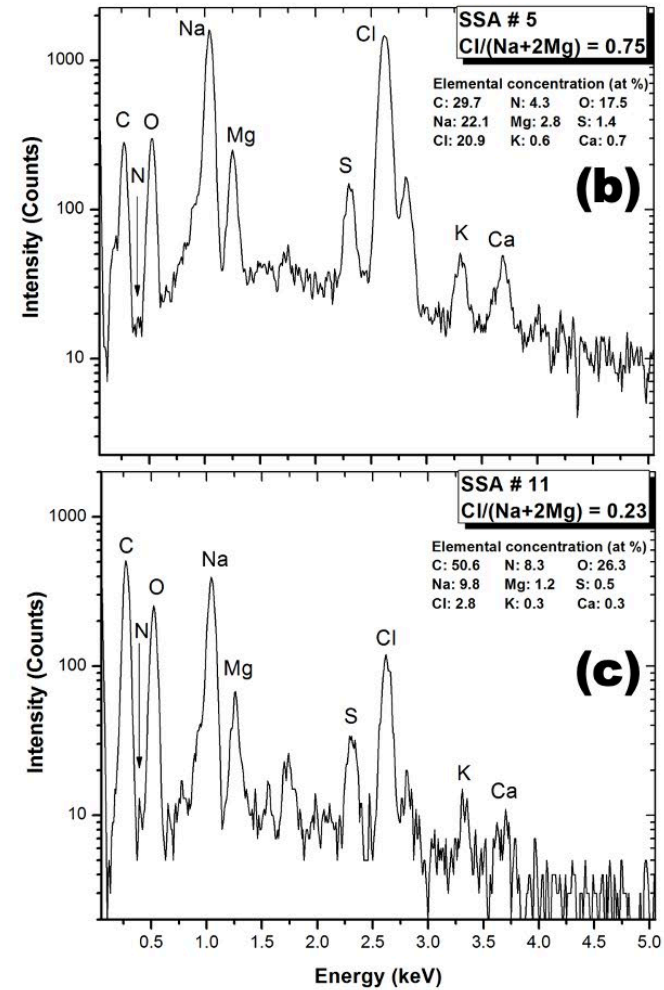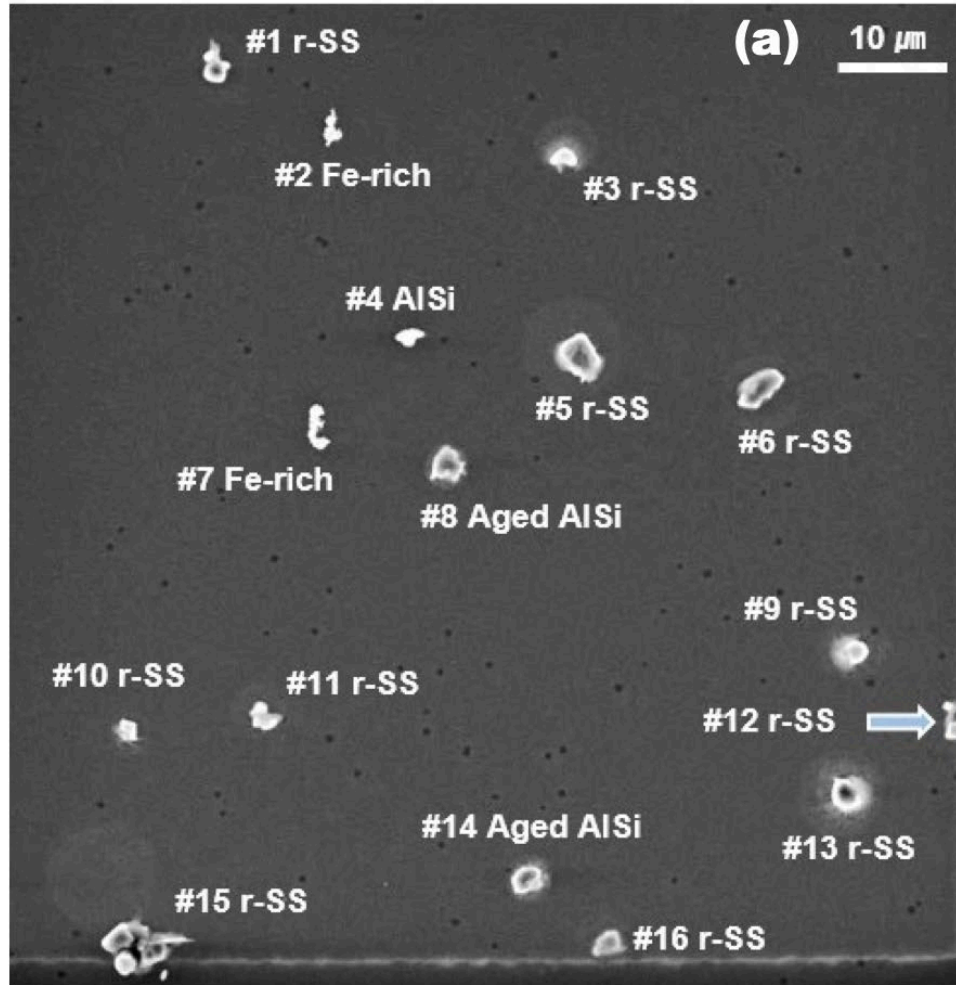
949

950

951 **Figure 3**. Optical images of the first field on TEM grid during humidifying (A-F, ↑) and dehydration (G-K, ↓) processes and the SEI
952 of the same field (L).
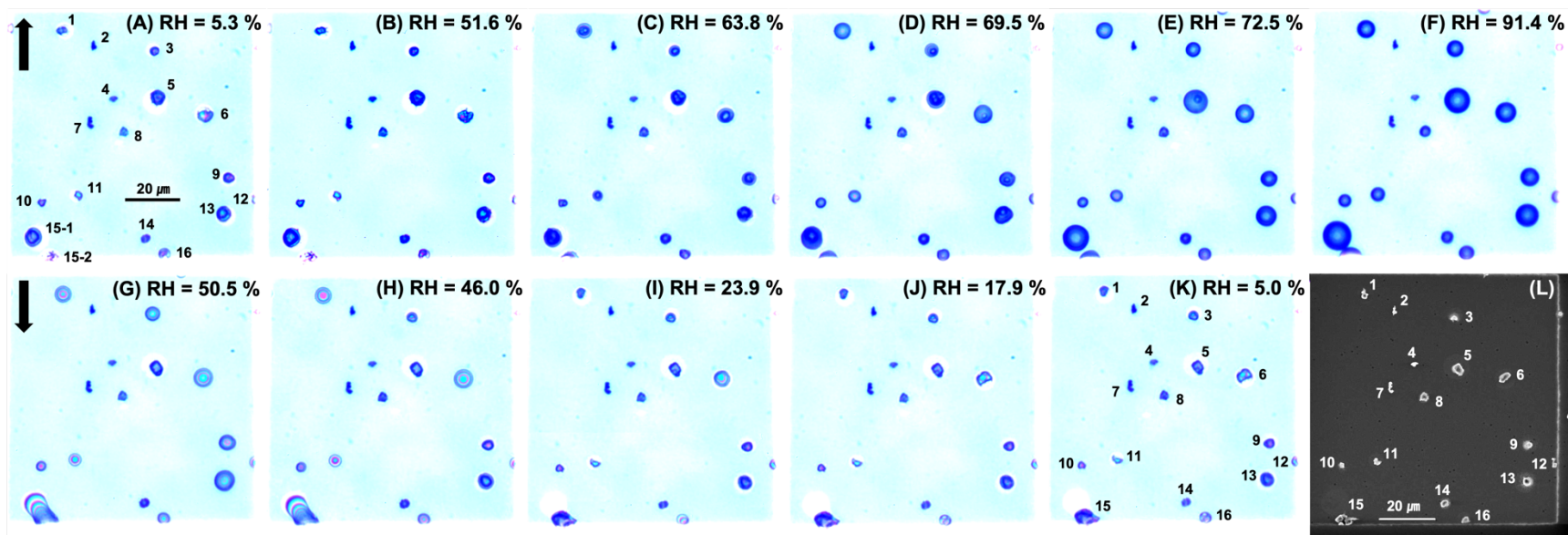
954 **Figure 4.** 2-D area ratio plot and optical images of Cl-rich SSAs #5 and #19 (a and d), 2-D area ratio plots of humidification (b and e)
955 and dehydration (c and f) for the SSAs and (Na,Mg)(Cl,NO₃) particle as a function of RH.
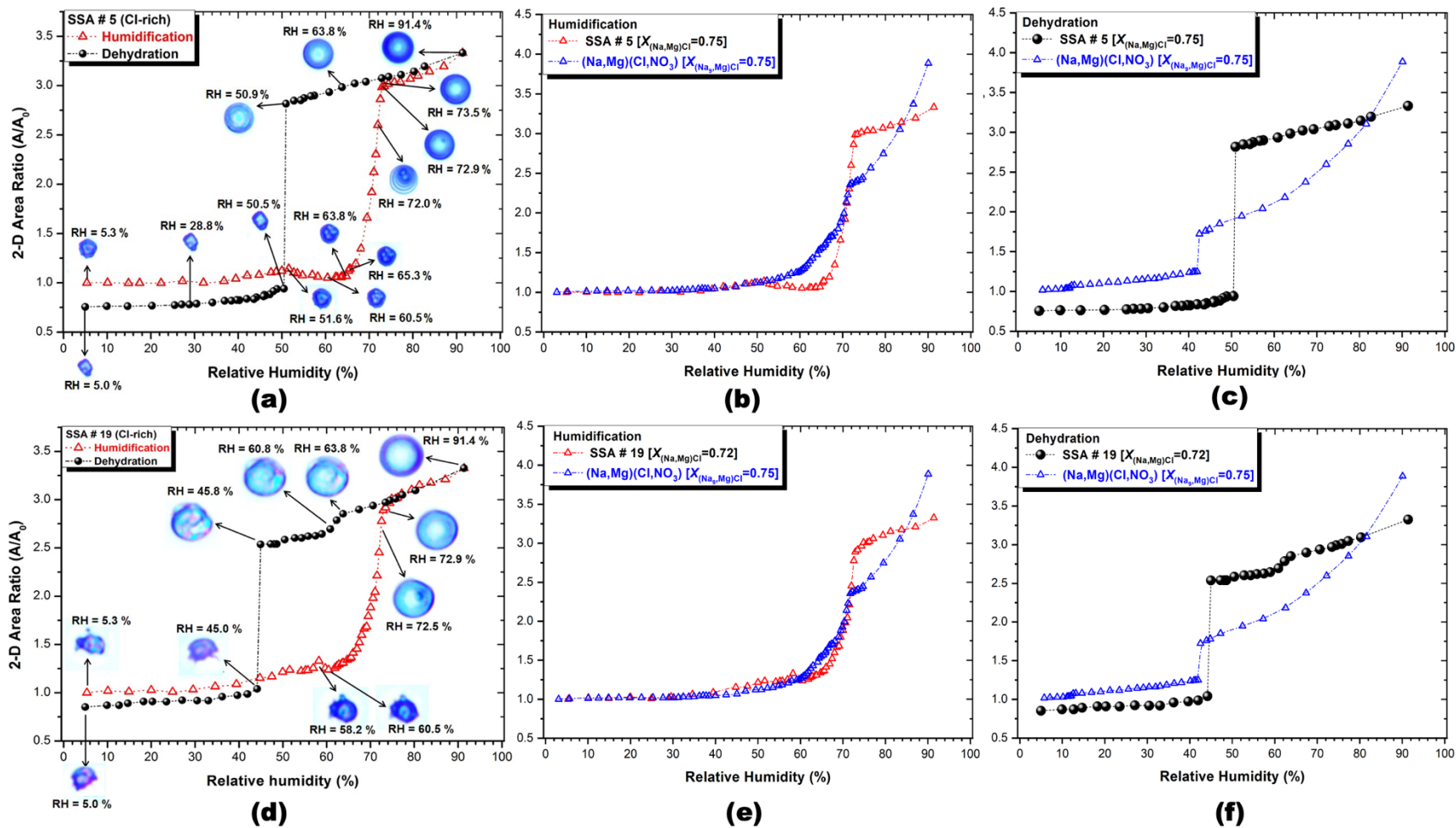
956

957

958

959 **Figure 5.** 2-D area ratio plot and optical images of an equimolar SSA #23 and a Cl-depleted SSA #11 (a and d), 2-D area ratio plots of
960 humidification (b and e) and dehydration (c and f) for the SSAs and (Na,Mg)(Cl,NO₃) particles as a function of RH.

961

962

963
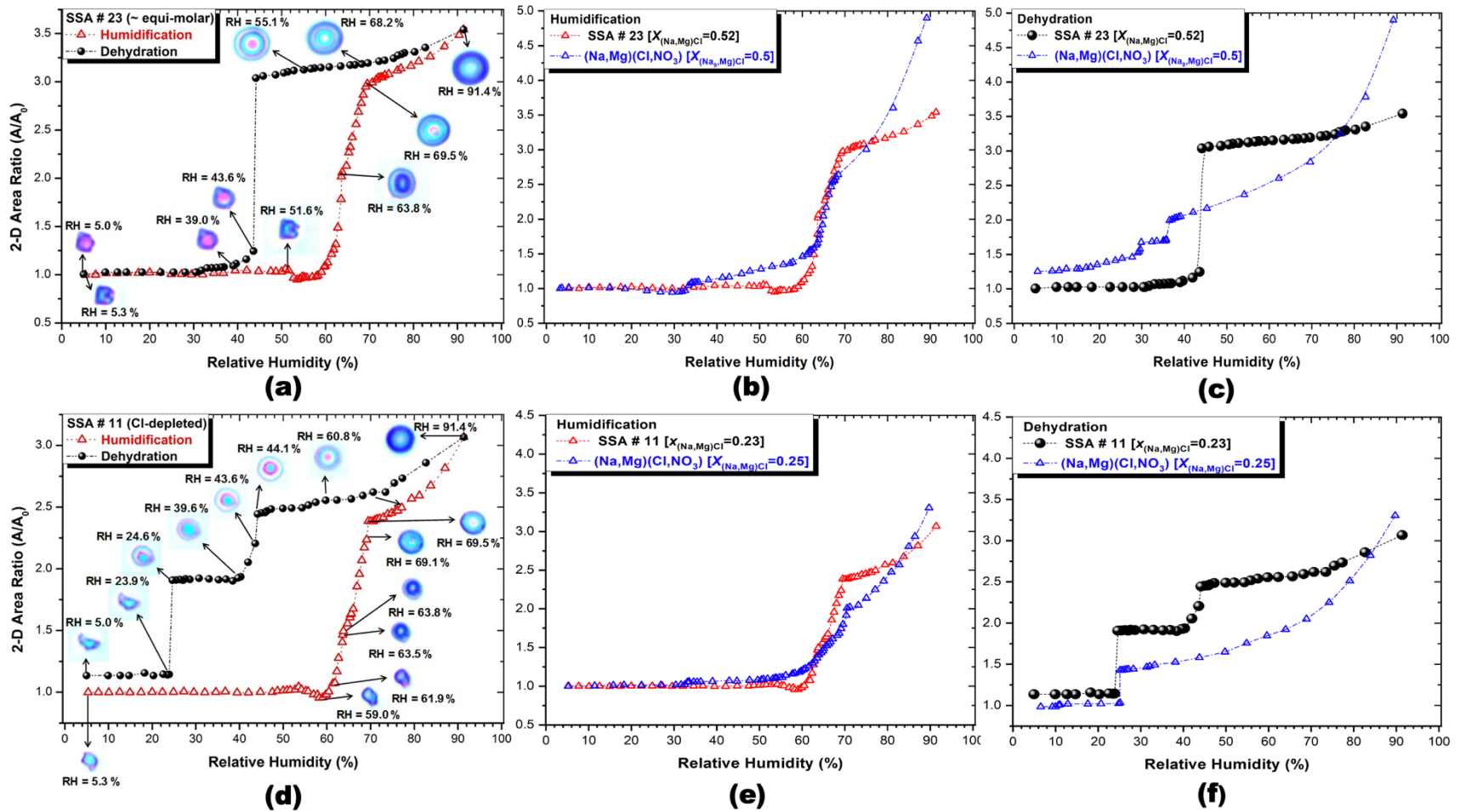
Figure 6. DRHs of ambient SSAs and (Na, Mg)(Cl, NO₃) and Na(Cl, NO₃) systems calculated from AIOMFAC plotted against the mole fraction of chloride [$X_{(Na, Mg)Cl}$ or X_{NaCl}]. Major chemical components in each phase: P - all in solid phase; Q - aqueous eutonic components + NaCl and (Na, Mg, Ca)(NO₃, SO₄, organics) in solid phase; R - NaNO₃ and (Ca, Na)SO₄ in solid phase + aqueous eutonic components; S - NaCl and (Ca, Na)SO₄ in solid phase + aqueous eutonic components; T - aqueous phase for most components; black vertical line – a eutonic composition of Na(Cl ,NO₃) system; blue vertical line – a eutonic composition of (Na, Mg)(Cl, NO₃) system.
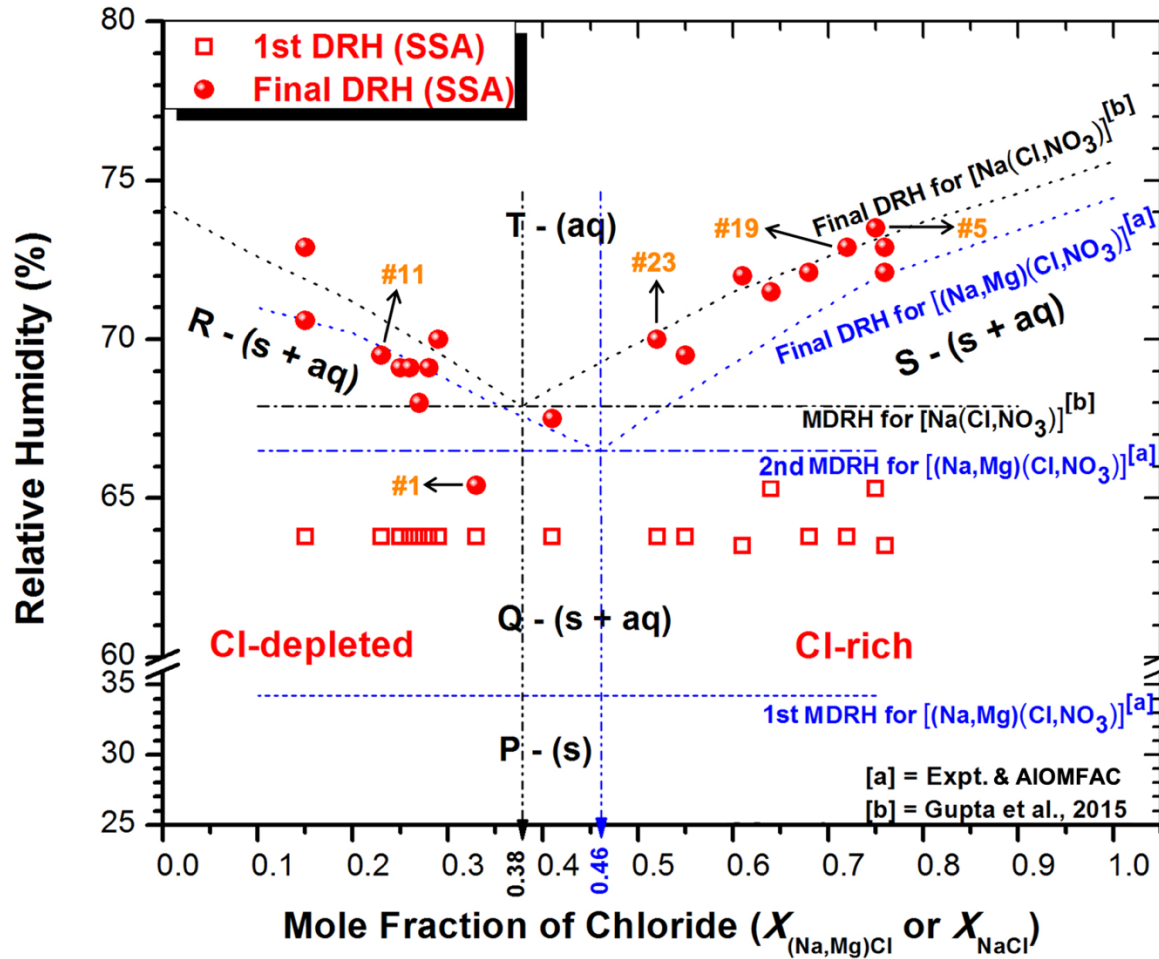
Figure 7. ERHs of ambient SSAs and those experimentally determined for (Na, Mg)(Cl, NO$_3$) and Na(Cl, NO$_3$) systems plotted against the mole fraction of chloride [$X_{(Na,Mg)Cl}$ or X_{NaCl}]. Major chemical components in each phase: P –almost all components in aqueous phase; Q - NaCl and other heterogeneously crystallized moieties in solid phase + aqueous nucleating species like (Mg·xH$_2$O)$^{2+}$ and Cl$^-$/NO$_3^-$/SO$_4^{2-}$; R - heterogeneously crystallized (Na, Mg)NO$_3$·xH$_2$O on crystalline (Ca, Na)SO$_4$(xH$_2$O) seeds + aqueous NaCl and other moieties; S - solid (Na, Mg, Ca)(NO$_3$, SO$_4$)·xH$_2$O and homogeneously crystallized NaCl + aqueous/amorphous (Mg·xH$_2$O)$^{2+}$ and NO$_3^-$/SO$_4^{2-}$, and other minor species; T - all in solid phase; black vertical line - a eutonic composition of Na(Cl ,NO$_3$) system; blue vertical line - a eutonic composition of (Na, Mg)(Cl, NO$_3$) system.
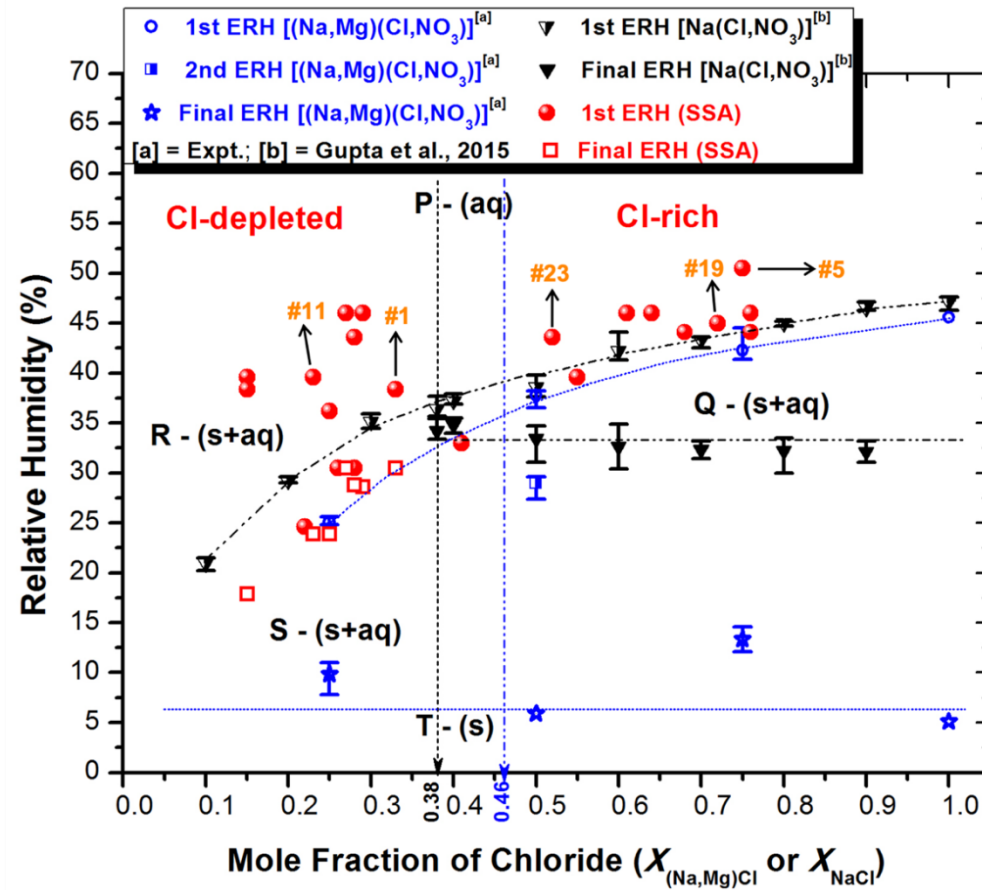
979 **Figure 8**. 2-D area ratio plot, X-ray spectrum, and SEM image with diameter of an aged aluminosilicate particle mixed with SSA (part
980 icle #14)

981

982